Available online at www.sciencedirect.com
SCIENCE DIRECT®
ELSEVIER
International Journal of Solids and Structures 43 (2006) 3983–4007
INTERNATIONAL JOURNAL OF SOLIDS and STRUCTURES
www.elsevier.com/locate/ijsolstr

Finite element analysis of post-buckling dynamics in plates—Part I: An asymptotic approach

Hui Chen, Lawrence N. Virgin *

Pratt School of Engineering, Duke University, Durham, NC 27708-0300, USA

Received 7 April 2005
Available online 23 June 2005

Abstract

Various static and dynamic aspects of post-buckled thin plates, including the transition of buckled patterns, post-buckling dynamics, secondary bifurcation, and dynamic snapping (mode jumping phenomenon), are investigated systematically using asymptotical and non-stationary finite element methods. In part I, the secondary dynamic instability and the local post-secondary buckling behavior of thin rectangular plates under generalized (mechanical and thermal) loading is investigated using an asymptotic numerical method which combines Koiter's nonlinear instability theory with the finite element technique. A dynamic multi-mode reduction method—similar to its static single-mode counterpart: Liapunov–Schmidt reduction—is developed in this perturbation approach. Post-secondary buckling equilibrium branches are obtained by solving the reduced low-dimensional parametric equations and their stability properties are determined directly by checking the eigenvalues of the resulting Jacobian matrix. Typical post-secondary buckling forms—transcritical, supercritical and subcritical bifurcations are observed according to different combinations of boundary conditions and load types. Geometric imperfection analysis shows that not only the secondary bifurcation load but also changes in the fundamental post-secondary buckling behavior are affected. The post-buckling dynamics and the global analysis of mode jumping of the plates are addressed in part II.

Keywords: Finite elements; Bifurcation; Frequencies; Mode jumping

1. Introduction

The phenomenon that thin plates under the action of elastic stresses may demonstrate a sudden dynamic change of their buckled modes when loaded deeply into the post-buckling regime is often called mode

* Corresponding author. Tel.: +1 919 660 5342; fax: +1 919 660 8963.
E-mail address: l.virgin@duke.edu (L.N. Virgin).

0020-7683/$ - see front matter © 2005 Elsevier Ltd. All rights reserved.
doi:10.1016/j.ijsolstr.2005.04.036

jumping. It has been proven to be of paramount importance in explaining a number of phenomena at many different scales. Examples may be found in biophysics (e.g. membrane shape, vesicle conformation, retina detachement (Audoly et al., 2002), mechanics (e.g. plate and isogrid panel deformation (Stein, 1959; Muheim and Johnson, 2003), film delamination (Audoly et al., 2002; Audoly, 2002; George et al., 2002)) and materials science (e.g. thermal barrier coatings and heteroepitaxial growth of microelectronic films (Sridhar et al., 2002, 2001)), to cite but a few.

It is a challenge to understand when such secondary instability will occur and how the buckled patterns will change their forms from one state on the primary stable equilibrium branch to another on a remote stable path. Initiated by Stein's experimental observation of such transient changes in the post-buckled deformation states in a compression test of a multi-bay, flat aluminum plate (Stein, 1959), many researches have been dedicated to the study of mode jumping of uniaxially compressed plates (Schaeffer and Golubitsky, 1979; Supple, 1968; Maaskant and Roorda, 1992; Uemura and Byon, 1977; Nakamura and Uetani, 1979; Stoll, 1994; Everall and Hunt, 1999a; Everall and Hunt, 1999b; Everall and Hunt, 2000; Hunt and Everall, 1999). A detailed review can be found in our previous paper (Chen and Virgin, 2004).

Bi-axially loaded plate models have recently been used to investigate the pattern formation and evolution of thin metal films and coatings sustaining high compressive stresses. George et al. (2002), use the energy variation method combined with the perturbation approach to study the delamination of an infinitely large thin film; the morphological change of buckled patterns—from strait-edge blisters to periodic distribution of droplets (or bumps)—has been observed. Audoly et al. (Audoly et al., 2002; Audoly, 2002), on the other hand, investigate the secondary buckling patterns of an infinitely long polycarbonate strip by solving the von Kármán equation using a modal analysis approach, where the configuration of the plate is assumed to consist of three fundamental modes: the strait-side blister mode, the bump mode and the antisymmetric droplets; various secondary buckling patterns have been predicted successfully and confirmed by their experimental data. Although the biaxial model can reveal some important characteristics of a thermally loaded plate, the real evolution of the nonlinear solutions of the latter cannot be analyzed accurately and the validity of the results need be checked.

Unlike its mechanically-loaded counterpart, mode jumping of a plate under thermal loading has by comparison received little attention, despite its significant applications in new materials and aerospace engineering. The main difficulty comes from the intensive coupling between the flexural deformation and *in-plane* boundary constraints. In this case, the external force is an implicit function of the vertical displacement, therefore it cannot be simply analogized by the uniformly distributed loads along edges. In Chen and Virgin (2004) and Virgin and Chen (2003), we made an initial study of this topic by investigating a thermally loaded thin plate with all its four edges simply supported and fixed in-plane. It was found that the plate under the action of thermal stress will demonstrate much stronger geometric nonlinearity than its mechanical counterpart. As a result the secondary bifurcation occurs far beyond the primary buckling point (e.g. the secondary buckling load can be as much as 46 times that of the initial buckling temperature (Chen and Virgin, 2004)). The analytical approach for predicting mode jumping cannot succeed even qualitatively unless sufficient modal components are taken into account. The propagation of the deformed configuration of the plate shows intricate yet intriguing pattern changes: before the occurrence of the secondary bifurcation, symmetric 'bump-like' patterns are developed smoothly, but after the snapping, an asymmetric oblique bump appears. Because of the strong nonlinearity presented, both the secondary instability and the pattern selection mechanisms of thin plates at high stresses still complicate analysis, in spite of the recent advances in nonlinear dynamics.

In the present study (part I and II), we aim at developing an efficient method to study the secondary instability and mode jumping of thin plates under more general load and boundary combinations. Numerical approaches such as the finite element method are well suited for this purpose. As mode jumping is often associated with the occurrence of the secondary instability, the study of the local behavior of structures near the secondary bifurcation point is by itself very important. Although the parametric continuation method now becomes the most versatile technique in analyzing nonlinear buckling of structures (Riks, 1984), at the

secondary bifurcation point where the primary path loses its stability, this method will encounter branch switching difficulties in determining the post-secondary buckling paths, especially for slender flexible structures such as plates, panels or shells. This is because slender structures often demonstrate complex unstable post-critical behaviors, characterized by strong mode interactions due to the occurrence of simultaneous or nearly simultaneous buckling modes. In this situation, perturbation methods are often used to investigate the local post-buckling behaviors.

In his pioneering work Koiter developed a general theory to analyze bifurcation problems in nonlinear elastic structures. It contains a blueprint for approaches to explore the initial post-buckling behavior of actual problems encountered in engineering practice. An excellent review can be found in Budiansky's presentation (Budiansky, 1974) and a comparison between the continuation method and the perturbation approach is given in Riks (1984). With the arrival of finite element techniques, many attempts have been made to reshape the method so that it can be implemented in general-purpose finite element codes. A computational method to calculate Koiter's *b*-factor, a measurement of the sensitivity to different kinds of imperfections of anisotropic panels is presented in Geier (2002). In Pignataro et al. (2000), the effect of interaction between one overall buckling mode and many local modes on the post-buckling behavior of uniformly compressed corrugated sheets is analyzed. Recently, Casciaro et al. (1991), Casciaro et al. (1992), Lanzo et al. (1995), Salernor and Casciaro (1997) and Lanzo and Garcea (1996) have developed a method which combines a modified perturbation approach with the use of a High-Continuity (HC) finite element and used it to analyze the post-buckling behavior of 3D trusses, rectangular plates and thin-walled structures. However, their derivations are limited to the mechanical loading case, where the external load is given explicitly. Moreover, equilibrium equations obtained by considering multi-mode interactions are simplified to cubic and quartic forms and the attractors (stable paths) are obtained by solving the appropriate reduced single-mode equations using minimum path theory. This is a very complicated procedure and there is some doubt as to whether, and to what extent, the separate single-mode analysis can represent a complete multi-mode analysis, especially for problems with stronger geometric nonlinearities.

In this paper, we will use a procedure similar to Casciaro's to develop an asymptotical method suitable for more general load cases. Nevertheless, the stability analysis of the post-secondary buckling branches is performed by introducing a dynamical multi-mode deduction method presented in Section 3. By changing the investigation from the static point of view (as did in most of previous researches) to that of dynamic, this method dramatically simplifies the procedure of the determination the post-buckling stability. Because mode jumping usually happens in the strongly nonlinear regime, in order to predict the initial post-secondary behavior accurately, the effect of initial imperfection is considered directly in the finite element model rather than approximated in the reduced equations as in many classical perturbation methods. A complete study of the post-buckling behavior of the generalized loaded plates, including the post-buckling dynamics and the global analysis of mode jumping of the plates, will be addressed in part II Chen and Virgin (in press) (Chen, 2004).

Here is a brief outline of this paper. In Section 2, basic static asymptotical equations based on Koiter's theory are derived by using the functional analysis approach. In Section 3, we introduce a multi-mode dynamical reduction method to study the stability of the local post-secondary bifurcation solutions. The finite element implementation of the resulting analytical equations is described in Section 4, whereas Section 5 is devoted to numerical analyses and discussions.

2. Perturbation theory and formulations

2.1. Equilibrium equation

Formally, a generalized displacement field u for a hyperelastic structure is sought by the application of the principle of stationary potential energy:

$$\delta\Pi[u;\lambda] = \Phi'[u(\lambda)]\delta u - \lambda\Psi'[u(\lambda)]\delta u = 0 \quad \forall\delta u \in \mathscr{T}, \tag{2.1}$$

where Π represents the total potential energy, Φ represents the strain energy of the elastic structure, Ψ represents the work done by the unit external force (mechanical or thermal load, for example), $\mathscr{T}$ represents the subspace of all admissible variations of the displacement u, the superscript $(\,)'$ denotes the Frechet derivative with respect to u, and the scalar variable λ represents the load parameter. Here it is also assumed that geometric constraints or boundary conditions are independent of λ.

For the mechanical loading case the unit load potential Ψ is linearly dependent on u, i.e., $\Psi = \hat{p}u$, where $\hat{p}$ denotes a unit mechanical loading pattern, while for the thermal case Ψ can be a nonlinear function of u because of the effect of boundary conditions.

Parameterizing both the solution u of the static equilibrium Eq. (2.1) and the load λ with respect to some path parameter, for example the arc-length s, gives $u = u(s)$, and $\lambda = \lambda(s)$. By taking the derivative of (2.1) with respect to s, the second order equilibrium equation can be obtained as

$$(\Phi''[u] - \lambda\Psi''[u])\breve{u}\delta u - \breve{\lambda}\Psi'[u]\delta u = 0, \quad \forall\delta u \in \mathscr{T}, \tag{2.2}$$

where the superscript $\breve{(\,)}$ represents differentiation with respect to s.

The critical situation occurs when Eq. (2.2) becomes singular:

$$(\Phi''_c - \lambda_c\Psi''_c)\breve{v}_c\delta u = 0, \quad \forall\delta u \in \mathscr{T}, \tag{2.3}$$

which gives two types of critical points (u_c, λ_c) on the equilibrium path—the limit point and bifurcation point, where $\breve{v}_c$ denotes the critical mode, $\Phi''_c = \Phi''[u(\lambda_c)]$, and $\Psi''_c = \Psi''[u(\lambda_c)]$.

The limit point is determined by $\Psi'_c\breve{v}_c \neq 0$ and $\breve{\lambda}_c = 0$, which gives a unique solution of (2.2): $\breve{u}_c = \breve{v}_c$, while the bifurcation point is determined by Fredholm's orthogonality condition, given by

$$\Psi'_c\breve{v}_c = 0, \quad \breve{\lambda}_c \neq 0, \tag{2.4}$$

and the non-unique solution $\breve{u}_c$ can be obtained as

$$\breve{u}_c = \breve{u}_p + \alpha_c\breve{v}_c, \tag{2.5}$$

where $\breve{u}_p$ is a particular solution of (2.2) and α_c is an arbitrary constant.

2.2. Perturbation algorithm

For a bifurcation problem, following from Koiter's theory, when $\lambda > \lambda_c$, the bifurcated equilibrium branch can be written as the summation of the fundamental path $u^f[\lambda]$ and a difference $v[\xi]$:

$$u[\lambda,\xi] = u^f[\lambda] + v[\xi], \quad \lambda = \lambda(\xi), \tag{2.6}$$

where ξ is a suitable parameter which measures the "amount" of buckling mode contained in the difference $u[\lambda,\xi] - u^f[\lambda]$ (Budiansky, 1974). Clearly, ξ vanishes at the bifurcation point, i.e., $\xi \to 0$ for $\lambda \to \lambda_b$. Note, from now on the subscript $(\,)_b$ is used to designate the evaluation of functions or variables at the bifurcation point (u_b, λ_b). As the fundamental path $u^f[\lambda]$ is assumed to be already known, the bifurcation path can be determined by using the Taylor expansion of $v[\xi]$ and $\lambda[\xi]$ at the bifurcation point and solving the following equilibrium equation:

$$(\Phi''[u[\lambda,\xi]] - \lambda\Psi'[u[\lambda,\xi]])\delta u = 0, \quad \forall\delta u \in \mathscr{T}. \tag{2.7}$$

Koiter's theory provides a rigorous method to analyze the initial post-bifurcation behavior of the structure. However, in practice, sometimes structures may present snap-through configurations, where bifurcation is not their natural character. In this limit point situation, a reference or artificial fundamental path needs to be constructed so that the snap-through behavior in the neighborhood of the limit point can be approxi-

mated by performing bifurcation analysis on the modified system. In this section, a modified general-purposed perturbation algorithm is developed to handle both of the above two problems.

Suppose that an equilibrium point (u_0, λ_0) near the true critical point[1] can be found on the fundamental configuration (this can be easily achieved, since in this paper we will use the arc-length method to obtain the fundamental path and (u_0, λ_0) can be given as the last stable point during the calculation), the fundamental path can be approximated by a quadratic extrapolation:

$$u^{\mathrm{f}}[\lambda] = u_0 + (\lambda - \lambda_0)\hat{u}_0 + \frac{1}{2}(\lambda - \lambda_0)^2\hat{\hat{u}}_0, \tag{2.8}$$

where the superscript $\hat{(\,)}$ designates the differentiation with respect to λ, $\hat{u}_0$ and $\hat{\hat{u}}_0$ denote the tangent and the curvature of the fundamental path at (u_0, λ_0), respectively. By substituting $u^{\mathrm{f}}[\lambda]$ into the equilibrium Eq. (2.1), taking the derivative with respect to λ once and twice, and evaluating the resulting equations at (u_0, λ_0), one may obtain $\hat{u}_0$ and $\hat{\hat{u}}_0$ by solving the following equations:

$$\Pi''_0\hat{u}_0\delta u - \Psi'_0\delta u = 0, \quad \forall \delta u \in \mathscr{T}, \tag{2.9}$$

$$\Pi''_0\hat{\hat{u}}_0\delta u + \Pi'''_0\hat{u}_0^2\delta u - 2\Psi''_0\hat{u}_0\delta u = 0, \quad \forall \delta u \in \mathscr{T}, \tag{2.10}$$

where $\Pi''_0 = \Phi''[u[\lambda_0]] - \lambda_0\Psi''[u[\lambda_0]], \Pi'''_0 = \Phi'''[u[\lambda_0]] - \lambda_0\Psi'''[u[\lambda_0]], \ldots$ The bifurcation point $(u_{\mathrm{b}}, \lambda_{\mathrm{b}})$ is therefore determined by

$$\Pi''[u^{\mathrm{f}}[\lambda_{\mathrm{b}}]]\breve{v}_{\mathrm{b}}\delta u = 0. \tag{2.11}$$

Immediately, one gets

$$\hat{u}_{\mathrm{b}} = \hat{u}_0 + (\lambda_{\mathrm{b}} - \lambda_0)\hat{\hat{u}}_0, \quad \hat{\hat{u}}_{\mathrm{b}} = \hat{\hat{u}}_0. \tag{2.12}$$

To simplify our derivation, from now on the unit load potential $\Psi[u]$ is assumed to be a quadratic function of the general displacement u or its derivatives, i.e., $\Pi'[u] = \Phi'[u] - \lambda\Psi'[u]$, $\Pi''[u] = \Phi''[u] - \lambda\Psi''[u]$, $\Pi'''[u] = \Phi'''[u]$, $\Pi^{(\mathrm{IV})}[u] = \Phi^{(\mathrm{IV})}[u], \ldots$

To this end, the bifurcated path is assumed to take the following form:[2]

$$u[\lambda, \xi] = u_{\mathrm{b}} + (\lambda - \lambda_{\mathrm{b}})\hat{u}_{\mathrm{b}} + \frac{1}{2}(\lambda - \lambda_{\mathrm{b}})^2\hat{\hat{u}}_{\mathrm{b}} + \xi\breve{v}_{\mathrm{b}} + \frac{1}{2}\xi^2\breve{\breve{w}}_{\mathrm{b}}, \tag{2.13}$$

where $\breve{(\,)}$ now represents the differentiation with respect to ξ; $\breve{v}_{\mathrm{b}}$ and $\breve{\breve{w}}_{\mathrm{b}}$ lie in two multi-orthogonal subspaces $\mathscr{V}$ and $\mathscr{W}$ defined by

$$\mathscr{T} = \mathscr{V} \oplus \mathscr{W},$$

$$\mathscr{V} = \{\alpha\breve{v}_{\mathrm{b}} | \forall \alpha \in \Re\} \quad \text{and} \quad \mathscr{W} = \{\breve{\breve{w}}_{\mathrm{b}} | \langle \breve{\breve{w}}_{\mathrm{b}}, \breve{v}_{\mathrm{b}} \rangle = 0, \forall \breve{\breve{w}}_{\mathrm{b}} \in \mathscr{T}\}, \tag{2.14}$$

where the inner product is defined explicitly by

$$\langle u, v \rangle = (\Phi'''_{\mathrm{b}}\hat{u}_{\mathrm{b}} - \Psi''_{\mathrm{b}})uv, \quad \forall u, v \in \mathscr{T}, \quad \text{with } \langle \breve{v}_{\mathrm{b}}, \breve{v}_{\mathrm{b}} \rangle = (\Phi'''_{\mathrm{b}}\hat{u}_{\mathrm{b}} - \Psi''_{\mathrm{b}})\breve{v}_{\mathrm{b}}^2 = -1. \tag{2.15}$$

[1] If the reference path $u^{\mathrm{f}}[\lambda]$ constructed from (u_0, λ_0) is close enough to the true equilibrium path which includes the limit point, a bifurcation point is guaranteed to exist on $u^{\mathrm{f}}[\lambda]$ (Casciaro et al., 1992).

[2] In fact, a more general expression

$$u[\lambda, \xi] = u_{\mathrm{b}} + (\lambda - \lambda_{\mathrm{b}})\hat{u}_{\mathrm{b}} + \frac{1}{2}(\lambda - \lambda_{\mathrm{b}})^2\hat{\hat{u}}_{\mathrm{b}} + \xi\breve{v}_{\mathrm{b}} + \xi(\lambda - \lambda_{\mathrm{b}})\hat{\breve{w}}_{\mathrm{b}} + \frac{1}{2}\xi^2\breve{\breve{w}}_{\mathrm{b}}$$

as suggested in Casciaro et al. (1991) for mechanical loading case ($\Psi[u] = \hat{p}u$) could have been used. However, after some mathematical manipulations, it can be proven that the middle term $\hat{\breve{w}}_{\mathrm{b}}$ actually vanishes even for the more general $\Psi[u]$.

Thus, the orthogonal condition can be expressed as

$$\langle \breve{v}_b, w\rangle = (\Phi'''_b \hat{u}_b - \Psi''_b)\breve{v}_b w = 0, \quad \forall w \in \mathscr{W}. \tag{2.16}$$

Substituting the expressions for fundamental path (2.8) and bifurcated path (2.13) into the equilibrium Eq. (2.1), respectively, performing the Taylor expansion at the bifurcation point, and projecting the resulting equations onto the orthogonal subspace $\mathscr{W}$, gives

$$\Pi''_b \breve{\breve{w}}_b \delta w + \Phi'''_b \breve{v}_b^2 \delta w = 0, \quad \forall \delta w \in \mathscr{W}, \quad \breve{\breve{w}} \in \mathscr{W}. \tag{2.17}$$

Note, in the above derivation use has been made of the bifurcation condition (2.3). The method of how to obtain the orthogonal term $\breve{\breve{w}}_b$ is left to Section 4.

The equilibrium path (with bifurcation or snap-through), determined by the nonlinear λ–ξ relationship, can be obtained by the application of the Liapunov–Schmidt–Koiter reduction procedure, in which the bifurcated path $u[\lambda, \xi]$ in (2.13) is substituted into the equilibrium Eq. (2.7) and then the resulting equation is projected in the direction of the buckling mode $\breve{v}_b$, i.e.,

$$(\Phi'[u[\lambda,\xi]] - \lambda\Psi'[u[\lambda,\xi]])\breve{v}_b = 0. \tag{2.18}$$

Substituting (2.13) into (2.18) and performing the Taylor expansion at (u_b, λ_b) gives

$$\begin{aligned}(\Phi'[u^f[\lambda]] - \lambda\Psi'[u^f[\lambda]])\breve{v}_b &+ \frac{1}{2}\xi^2\Phi'''_b\breve{u}_b^3 + \xi(\lambda-\lambda_b)(\Phi'''_b\hat{u}_b - \Psi''_b)\breve{v}_b^2 + \frac{1}{2}(\lambda-\lambda_b)^2\xi[\Phi_b^{(IV)}\hat{u}_b^2\breve{v}_b^2 + \Phi'''_b\hat{u}_b\breve{v}_b^2] \\ &+ \frac{1}{2}(\lambda-\lambda_b)\xi^2[\Phi_b^{(IV)}\hat{u}_b\breve{v}_b^3 + \Phi'''_b\breve{\breve{w}}_b\hat{u}_b\breve{v}_b - \Psi''_b\breve{\breve{w}}_b\breve{v}_b] + \frac{1}{6}\xi^3(\Phi^{(IV)}\breve{v}_b^4 + 3\Phi'''_b\breve{\breve{w}}_b\breve{\breve{v}}_b^2) + O(\xi^4) = 0.\end{aligned} \tag{2.19}$$

The first term in the above equation is the load residual of the bifurcation path $u^f[\lambda]$ and generally $(\Phi'[u^f[\lambda]] - \lambda\Psi'[u^f[\lambda]])\breve{v}_b \neq 0$. It vanishes only at the starting point (u_0, λ_0). For a bifurcation problem, (u_0, λ_0) may be coincident with (u_b, λ_b). By using the Taylor expansion further on the load residual term and taking advantage of (2.16) and (2.17), the bifurcation Eq. (2.19) can be simplified to

$$g(\lambda,\xi) = h_l(\lambda) + A_3(\lambda-\lambda_b)\xi + \frac{1}{2}A_4\xi^2 + \frac{1}{2}A_5(\lambda-\lambda_b)^2\xi + \frac{1}{2}A_6(\lambda-\lambda_b)\xi^2 + \frac{1}{6}A_7\xi^3 + O(\xi^4) = 0, \tag{2.20}$$

where

$$h_l(\lambda) = \frac{1}{2}A_1(\lambda-\lambda_0)^2 + \frac{1}{6}A_2(\lambda-\lambda_0)^2(\lambda+2\lambda_0-3\lambda_b), \tag{2.21}$$

$$\begin{aligned}&A_1 = \Phi'''_b\hat{u}_b^2\breve{v}_b - 2\Psi''_b\hat{u}_b\breve{v}_b, \quad A_2 = \Phi_b^{(IV)}\hat{u}_b^3\breve{v}_b + 3(\Phi'''_b\hat{u}_b - \Psi''_b)\hat{\hat{u}}_b\breve{v}_b, \\ &A_3 = -1, \quad A_4 = \Phi'''_b\breve{v}_b^3, \quad A_5 = \Phi_b^{(IV)}\hat{u}_b^2\breve{v}_b^2 + \Phi'''_b\hat{\hat{u}}_b\breve{v}_b^2, \\ &A_6 = \Phi_b^{(IV)}\hat{u}_b\breve{v}_b^3, \quad A_7 = \Phi_b^{(IV)}\breve{v}_b^4 - 3\Pi''_b\breve{\breve{w}}_b^2.\end{aligned} \tag{2.22}$$

The bifurcation Eq. (2.20) can be used to study all possible behavior of the structure in the immediate neighborhood of the critical state (u_b, λ_b) for small $\lambda - \lambda_b$ and ξ. To study the most commonly encountered bifurcation types in elastic structures, (2.20) can be written in a shortened form:

$$g(\lambda,\xi) = C_0 + C_1\Delta\lambda + C_2\xi\Delta\lambda + C_3\xi^2 + C_4\xi^3, \tag{2.23}$$

where $\Delta\lambda = (\lambda - \lambda_b)$, and

$$\begin{aligned}&C_0 = \frac{1}{2}(\lambda_b-\lambda_0)^2A_1 - \frac{1}{3}(\lambda_b-\lambda_0)^3A_2, \quad C_1 = (\lambda_b-\lambda_0)\left(A_1 - \frac{A_2(\lambda_b-\lambda_0)}{2}\right), \\ &C_2 = -1, \quad C_3 = \frac{1}{2}A_4, \quad C_4 = \frac{1}{6}A_7.\end{aligned} \tag{2.24}$$

Now we are able to resort to the criteria presented in Riks et al.'s paper (Riks et al., 1996) to determine the following four types of bifurcation behavior:

$$\begin{aligned}
&\text{Limit Point :} && C_1 < 0, \quad C_3 < 0;\\
&\text{Asymmetric bifurcation point :} && C_1 = 0, \quad C_2 < 0, \quad C_3 \neq 0;\\
&\text{Symmetric bifurcation point(subcritical) :} && C_1 = 0, \quad C_2 < 0, \quad C_3 = 0, \quad C_4 < 0;\\
&\text{Symmetric bifurcation point(supercritical) :} && C_1 = 0, \quad C_2 < 0, \quad C_3 = 0, \quad C_4 > 0.
\end{aligned} \tag{2.25}$$

3. Multi-mode dynamic reduction

The analysis in Section 2 is based on an implicit hypothesis that the initial post-buckling behavior is dominated by the lowest critical mode $\breve{v}_b$ determined by (2.11). However, for plates or structures composed of slender panels, there exists a cluster of isolated close-by bifurcation points on the fundamental path. In this situation, the buckled equilibrium paths are greatly affected by the strong interactions among the buckling modes corresponding to these competitive eigenvalues. Therefore the post-secondary buckling behavior, which is especially important for understanding the mode-jumping phenomenon, cannot be predicted correctly with such a single-mode model.

Another important issue for determining the mode-jumping is to analyze the stability of the various post-buckled equilibrium paths branching from the fundamental one. Recently, two stability analysis methods have been developed based on the minimum path theory. In Riks et al. (1996), the stability of the critical point for the discrete system is studied. Alternatively, in Salernor and Casciaro (1997) and Lanzo and Garcea (1996), equilibrium equations obtained by considering multi-mode interactions are simplified to cubic and quartic forms and the attractors (stable paths) are obtained by solving the appropriate reduced single-mode equations. However, both the above methods are based on static analysis and, as mentioned before, the latter approach is very complicated and there is doubt over whether the separate single-mode analysis can represent a complete multi-mode analysis.

In this section, we will introduce a simple and effective multi-mode dynamic reduction method to study the stability of the post-buckled branches dynamically.

The dynamic equation and all the boundary conditions for a complete system can be derived from an application of Hamilton's principle:

$$\delta \int_{t_1}^{t_2} [K[\dot{u}] - (\Phi[u] - \lambda \Psi[u])] \mathrm{d}t = 0, \tag{3.1}$$

$$\delta u(t_1) = \delta u(t_2) = 0, \tag{3.2}$$

where $K = \frac{1}{2}\int_\Omega \rho \dot{u}^2 \,\mathrm{d}\Omega$ represents the kinetic energy and the overdot $(\dot{})$ represents the derivative with respect to the time t. Integrating the equation by parts gives

$$\int_{t_1}^{t_2} \left\{ \left[\int_\Omega \rho \ddot{u} \,\mathrm{d}\Omega + (\Phi'[u] - \lambda \Psi'[u]) \right] \delta u + \int_{\partial\Omega} \text{Boundary conditions } \delta u \right\} \mathrm{d}t = 0, \quad \forall \delta u \in \mathscr{T}. \tag{3.3}$$

The governing equation thus takes the form of

$$\left[\int_\Omega \rho \ddot{u} \,\mathrm{d}\Omega + (\Phi'[u] - \lambda \Psi'[u]) \right] \delta u = 0, \quad \forall \delta u \in \mathscr{T}. \tag{3.4}$$

Supposing that there exist M distinct close-by bifurcation points on the fundamental path $u^f[\lambda]$, the bifurcation condition now becomes

$$\Pi''[u^{\mathrm{f}}[\lambda_{\mathrm{b}i}]]\breve{v}_{\mathrm{b}i}\delta u = 0, \quad \forall \delta u \in \mathscr{T}, \quad i = 1, 2, \ldots, M, \tag{3.5}$$

where $\breve{v}_{\mathrm{b}i}$ is the eigenvector corresponding to the eigenvalue $\lambda_{\mathrm{b}i}$. The nominal bifurcation point is still $(\lambda_{\mathrm{b}}, u_{\mathrm{b}})$, which is chosen from the $\lambda_{\mathrm{b}i}$'s and typically is the smallest eigenvalue. The above nonlinear eigenvalue problem can be solved by linearizing (3.5) at $(\lambda_{\mathrm{b}}, u_{\mathrm{b}})$:

$$\Pi''_{\mathrm{b}}\breve{v}_{\mathrm{b}i}\delta u + (\lambda_{\mathrm{b}i} - \lambda_{\mathrm{b}})(\Phi'''_{\mathrm{b}}\hat{u}_{\mathrm{b}} - \Psi''_{\mathrm{b}})\breve{v}_{\mathrm{b}i}\delta u = 0, \quad \forall \delta u \in \mathscr{T}. \tag{3.6}$$

From (3.6), it is easy to prove that these M distinct eigenvectors are in fact orthogonal to each other with respect to the inner product defined in (2.15) and can be normalized as

$$(\Phi'''_{\mathrm{b}}\hat{u}_{\mathrm{b}} - \Psi''_{\mathrm{b}})\breve{v}_{\mathrm{b}i}\breve{v}_{\mathrm{b}j} = \begin{cases} 0, & i \neq j; \\ -1, & i = j \text{ and } \lambda_{\mathrm{b}i} \geqslant \lambda_{\mathrm{b}}; \\ 1, & i = j \text{ and } \lambda_{\mathrm{b}i} < \lambda_{\mathrm{b}}. \end{cases} \tag{3.7}$$

Consequently,

$$\Pi''_{\mathrm{b}}\breve{v}_{\mathrm{b}i}\breve{v}_{\mathrm{b}j} = \begin{cases} 0, & \text{for } i \neq j; \\ |\lambda_{\mathrm{b}i} - \lambda_{\mathrm{b}}|, & \text{for } i = j. \end{cases} \tag{3.8}$$

Similar to the previous static single-mode analysis, the bifurcated path is now assumed to take the following form:

$$u[\lambda, \boldsymbol{\xi}, t] = u^{\mathrm{f}}[\lambda(t)] + \sum_{i=1}^{M} \xi_i(t)\breve{v}_{\mathrm{b}i} + \frac{1}{2}\sum_{i=1}^{M}\sum_{j=1}^{M} \xi_i(t)\xi_j(t)\breve{\breve{w}}_{ij}, \tag{3.9}$$

where $\boldsymbol{\xi} = [\xi_1, \xi_2, \ldots, \xi_M]$, $\breve{v}_{\mathrm{b}i} \in \mathscr{V}$ and $\breve{\breve{w}}_{ij} \in \mathscr{W}$ with two orthogonal subspaces $\mathscr{V}$ and $\mathscr{W}$ now defined as

$$\mathscr{V} = \left\{ \sum_{i=1}^{M} \alpha_i \breve{v}_{\mathrm{b}i} | \forall \alpha_i \in \Re \right\} \quad \text{and} \quad \mathscr{W} = \{\breve{\breve{w}}_{ij} | \langle \breve{\breve{w}}_{ij}, \breve{v}_{\mathrm{b}i} \rangle = 0, \forall \breve{v}_{\mathrm{b}i} \in \mathscr{V}, \breve{\breve{w}}_{ij} \in \mathscr{T}\}. \tag{3.10}$$

The orthogonality condition in (2.16) can be rewritten as

$$\langle \breve{v}_{\mathrm{b}i}, w \rangle = (\Phi'''_{\mathrm{b}}\hat{u}_{\mathrm{b}} - \Psi''_{\mathrm{b}})\breve{v}_{\mathrm{b}i}w = 0, \quad \forall w \in \mathscr{W}, \quad i = 1, 2, \ldots, M. \tag{3.11}$$

From (3.9), we observe that the fundamental path $u^{\mathrm{f}}[\lambda(t)]$ can only be achieved if all $\xi_i(t) = 0$, $i = 1,2, \ldots, M$; for any $\xi_i(t) \neq 0$, (3.9) designates a bifurcation path. Since the stability of the fundamental equilibrium path is already known, we are only concerned with the dynamical stability of the bifurcated equilibrium paths (the stationary solutions of (3.4)).

To achieve this goal, we now adopt a quasi-dynamical approach—assume that the load λ is increased quasi-statically, i.e., $\dot{\lambda}(t) = \lambda$, therefore the fundamental path $u^{\mathrm{f}}[\lambda]$ in (3.9) only serves as a fixed reference path and any small perturbation on the bifurcated paths is automatically reflected by small variations of $\xi_i(t)$'s from their equilibrium values. As a result, the dynamical stability (in Liapunov's sense) of the bifurcated paths can be obtained by analyzing the dynamical equations with respect to the $\xi_i(t)$'s.

By considering $\dot{\lambda}(t) = \lambda$, the acceleration of u (second time derivative of u) can be obtained from (3.9) as

$$\ddot{u}[\lambda, \boldsymbol{\xi}(t)] = \sum_{i=1}^{M} \left(\breve{v}_{\mathrm{b}i} + \frac{1}{2}\sum_{j=1}^{M} (\breve{\breve{w}}_{ij} + \breve{\breve{w}}_{ji})\xi_j(t) \right) \ddot{\xi}_i(t) + \sum_{i=1}^{M}\sum_{j=1}^{M} \breve{\breve{w}}_{ij}\dot{\xi}_i(t)\dot{\xi}_j(t). \tag{3.12}$$

Note, the stationary solution of (3.4) is still governed by (2.7). Substituting the stationary equilibrium path $u^{\mathrm{f}}[\lambda]$ and $u[\lambda, \boldsymbol{\xi}]$ into (2.1), respectively, using Taylor expansion at $(u_{\mathrm{b}}, \lambda_{\mathrm{b}})$ and projecting the resulting equations onto the orthogonal subspace $\mathscr{W}$, one gets

$$\sum_{i=1}^{M}\xi_i[\Pi''_{\mathrm{b}}\breve{v}_{\mathrm{b}i}+(\lambda-\lambda_{\mathrm{b}})(\Phi'''_{\mathrm{b}}\hat{u}_{\mathrm{b}}-\Psi''_{\mathrm{b}})\breve{v}_{\mathrm{b}i}]\delta w+\frac{1}{2}\sum_{i=1}^{M}\sum_{j=1}^{M}\xi_i\xi_j[\Pi''_{\mathrm{b}}\breve{\breve{w}}_{ij}\delta w+\Phi'''_{\mathrm{b}}\breve{v}_{\mathrm{b}i}\breve{v}_{\mathrm{b}j}\delta w]+\cdots=0. \tag{3.13}$$

According to (3.6), the first term in the above equation vanishes automatically. The orthogonal term $\breve{\breve{w}}_{ij}$ thus can be determined by solving

$$\Pi''_{\mathrm{b}}\breve{\breve{w}}_{ij}\delta w+\Phi'''_{\mathrm{b}}\breve{v}_{\mathrm{b}i}\breve{v}_{\mathrm{b}j}\delta w=0,\quad \breve{\breve{w}}_{ij}\in\mathscr{W},\quad \forall\delta w\in\mathscr{W}. \tag{3.14}$$

With $\breve{\breve{w}}_{ij}$ being solved in the orthogonal subspace $\mathscr{W}$, the reduced order dynamic equations can be obtained by projecting Eq. (3.4) into the bifurcated subspace $\mathscr{V}$, i.e.,

$$\left(\int_{\Omega}\rho\ddot{u}[\lambda,\boldsymbol{\xi}(t)]\mathrm{d}\Omega\right)\breve{v}_{\mathrm{b}l}+(\Phi'[u[\lambda,\boldsymbol{\xi}(t)]]-\lambda\Psi'[u[\lambda,\boldsymbol{\xi}(t)]])\breve{v}_{\mathrm{b}l}=0,\quad l=1,2,\ldots,M. \tag{3.15}$$

Since our goal is not to solve the dynamical Eq. (3.15) but to determine the linear stability of the bifurcated equilibrium path, the nonlinear terms in (3.12) can be dropped which gives

$$\sum_{i=1}^{M}(int_{\Omega}\rho\breve{v}_{\mathrm{b}i}\breve{v}_{\mathrm{b}l}\mathrm{d}\Omega)\ddot{\xi}_i(t)+g_l[\lambda,\boldsymbol{\xi}(t)]=0,\quad l=1,2,\ldots,M, \tag{3.16}$$

where

$$g_l[\lambda,\boldsymbol{\xi}(t)]=(\Phi'[u[\lambda,\boldsymbol{\xi}(t)]]-\lambda\Psi'[u[\lambda,\boldsymbol{\xi}(t)]])\breve{v}_{\mathrm{b}l}. \tag{3.17}$$

Applying a Taylor expansion to (3.17) at $(\lambda_{\mathrm{b}},u_{\mathrm{b}})$ gives

$$\begin{aligned}g_l[\lambda,\boldsymbol{\xi}(t)]=&h_l(\lambda)-\mathrm{sign}(\lambda_{\mathrm{b}l}-\lambda_{\mathrm{b}})(\lambda-\lambda_{\mathrm{b}l})\xi_l(t)+\frac{1}{2}\sum_{i=1}^{M}\sum_{j=1}^{M}\xi_i(t)\xi_j(t)R_{ijl}\\&+\frac{1}{2}(\lambda-\lambda_{\mathrm{b}})^2\sum_{i=1}^{M}\xi_i(t)S_{il}+\frac{1}{2}(\lambda-\lambda_{\mathrm{b}})\sum_{i=1}^{M}\sum_{j=1}^{M}\xi_i(t)\xi_j(t)T_{ijl}\end{aligned} \tag{3.18}$$

$$+\frac{1}{6}\sum_{i=1}^{M}\sum_{j=1}^{M}\sum_{k=1}^{M}\xi_i(t)\xi_j(t)\xi_k(t)W_{ijkl}+\mathrm{HOT}, \tag{3.19}$$

where

$$h_l[\lambda]=(\Phi'[u^{\mathrm{f}}[\lambda]]-\lambda\Psi'[u^{\mathrm{f}}[\lambda]])\breve{v}_{\mathrm{b}l},\quad l=1,2,\ldots,M, \tag{3.20}$$

$$\begin{aligned}R_{ijl}&=\Phi'''_{\mathrm{b}}\breve{v}_{\mathrm{b}i}\breve{v}_{\mathrm{b}j}\breve{v}_{\mathrm{b}l},\\S_{il}&=\Phi^{(\mathrm{IV})}_{\mathrm{b}}\hat{u}^2_{\mathrm{b}}\breve{v}_{\mathrm{b}i}\breve{v}_{\mathrm{b}l}+\Phi'''_{\mathrm{b}}\hat{\hat{u}}_{\mathrm{b}}\breve{v}_{\mathrm{b}i}\breve{v}_{\mathrm{b}l},\\T_{ijl}&=\Phi^{(\mathrm{IV})}_{\mathrm{b}}\hat{u}_{\mathrm{b}}\breve{v}_{\mathrm{b}i}\breve{v}_{\mathrm{b}j}\breve{v}_{\mathrm{b}l},\\W_{ijkl}&=\Phi^{(\mathrm{IV})}_{\mathrm{b}}\breve{v}_{\mathrm{b}i}\breve{v}_{\mathrm{b}j}\breve{v}_{\mathrm{b}k}\breve{v}_{\mathrm{b}l}-3\Pi''_{\mathrm{b}}\breve{\breve{w}}_{ij}\breve{\breve{w}}_{kl}.\end{aligned} \tag{3.21}$$

Note, in the above derivation, use has been made of the following two equations:

$$\Pi''_{\mathrm{b}}\breve{v}_{\mathrm{b}i}\breve{v}_{\mathrm{b}l}+(\lambda-\lambda_{\mathrm{b}})(\Phi'''_{\mathrm{b}}\hat{u}_{\mathrm{b}}-\Psi''_{\mathrm{b}})\breve{v}_{\mathrm{b}i}\breve{v}_{\mathrm{b}l}=\begin{cases}0, & \text{if } l\neq i,\\-(\lambda-\lambda_{\mathrm{b}l}), & \text{if } l=i, \text{ and } \lambda_{\mathrm{b}l}\geqslant\lambda_{\mathrm{b}},\\(\lambda-\lambda_{\mathrm{b}l}), & \text{if } l=i, \text{ and } \lambda_{\mathrm{b}l}<\lambda_{\mathrm{b}},\end{cases} \tag{3.22}$$

$$\Pi''_{\mathrm{b}}\breve{v}_{\mathrm{b}l}\breve{\breve{w}}_{ij}=0,\quad i,j,l=1,2,\ldots,M. \tag{3.23}$$

The physical meaning of the expression $h_l[\lambda]$ is that it represents the projection of the residual (caused by substituting the approximated fundamental path into the equilibrium equation) in the direction of $\breve{v}_{bl}$. By further using Taylor expansion at the nominal bifurcation point, expression $h_l[\lambda]$ is thus given as

$$h_l[\lambda] = \frac{1}{2}(\lambda-\lambda_0)^2[\Pi''_b\hat{\hat{u}}_b\breve{v}_{bl} + (\Phi'''_b\hat{u}_b - 2\Psi''_b)\hat{u}_b\breve{v}_{bl}] + \frac{1}{6}(\lambda-\lambda_0)^2(\lambda+2\lambda_0-3\lambda_b)[\Phi^{(IV)}_b\hat{u}^3_b\breve{v}_{bl} + 3(\Phi'''_b\hat{u}_b - \Psi''_b)\hat{\hat{u}}_b\breve{v}_{bl}] + \text{HOT}. \tag{3.24}$$

By letting $\boldsymbol{\xi}(t) = \{\xi_1(t), \xi_2(t)\ldots,\xi_M(t)\}^T$ and $\mathbf{g}(\lambda,\boldsymbol{\xi}) = \{g_1(\lambda,\boldsymbol{\xi}), g_2(\lambda,\boldsymbol{\xi})\ldots,g_M(\lambda,\boldsymbol{\xi})\}^T$, the dynamical Eq. (3.15) can be written in matrix form:

$$\mathbf{A}\ddot{\boldsymbol{\xi}}(t) + \mathbf{g}(\lambda,\boldsymbol{\xi}(t)) = \mathbf{0}, \tag{3.25}$$

with components of $\mathbf{A}$ defined by $A_{ij} = \int_\Omega \rho\breve{v}_{bi}\breve{v}_{bj}\,d\Omega$. By further introducing finite element discretization, the buckling mode can be expressed as $\breve{v}_{bi} = \mathbf{N}\mathbf{d}_i$, $\mathbf{d}_i \in \Re^N$, where $\mathbf{N}$ and $\mathbf{d}_i$ are the shape function and the nodal value of v_{bi}, respectively. To this end, the matrix $\mathbf{A}$ can be rewritten in the following form:

$$\mathbf{A} = \begin{bmatrix} \mathbf{d}_1^T\mathbf{M}\mathbf{d}_1 & \mathbf{d}_1^T\mathbf{M}\mathbf{d}_2 & \cdots & \mathbf{d}_1^T\mathbf{M}\mathbf{d}_M \\ \mathbf{d}_2^T\mathbf{M}\mathbf{d}_1 & \mathbf{d}_2^T\mathbf{M}\mathbf{d}_2 & \cdots & \mathbf{d}_2^T\mathbf{M}\mathbf{d}_M \\ \cdots & \cdots & \cdots & \cdots \\ \mathbf{d}_M^T\mathbf{M}\mathbf{d}_1 & \mathbf{d}_M^T\mathbf{M}\mathbf{d}_2 & \cdots & \mathbf{d}_M^T\mathbf{M}\mathbf{d}_M \end{bmatrix} = \mathbf{S}^T\mathbf{M}\mathbf{S}, \tag{3.26}$$

where $\mathbf{M} = \int_\Omega \rho\mathbf{N}^T\mathbf{N}\,d\Omega$ is the mass matrix of the discrete system and $\mathbf{S} = \{\mathbf{d}_1, \mathbf{d}_2, \ldots, \mathbf{d}_M\}$ can be considered as a transformation matrix which reduces the nonlinear dynamic problem in the high-dimensional displacement space to the low-dimensional parametrical space. The multi-orthogonal property of the column vectors in $\mathbf{S}$ comes from (3.8). Since $\mathbf{M}$ is positive definite, it is easy to prove that the reduced mass matrix $\mathbf{A}$ is also positive definite. In fact, $\forall\boldsymbol{\xi}_x \in \Re^M$, $\boldsymbol{\xi}_x \neq \mathbf{0}$, $\boldsymbol{\xi}_x^T\mathbf{A}\boldsymbol{\xi}_x = (\mathbf{S}\boldsymbol{\xi}_x)^T\mathbf{M}(\mathbf{S}\boldsymbol{\xi}_x) > 0$. Therefore, the stability of the equilibrium solutions of (3.25) is indeed determined only by the Jacobian of $\mathbf{g}(\lambda,\boldsymbol{\xi})$. That is, for a specific stationary solution $(\lambda_0,\boldsymbol{\xi}_0)$ of (3.25), it is stable if the Jacobian matrix $\mathbf{D}\mathbf{g}(\lambda,\boldsymbol{\xi})|_{(\lambda_0,\boldsymbol{\xi}_0)}$ is positive definite, otherwise, the solution is dynamically unstable.

Eq. (3.25) not only dramatically simplifies the procedure of calculating the post-buckled equilibrium paths and determining their stability but also provides an efficient way of approximating the lowest M natural frequencies. If seeking the equilibrium and determining the stability are the only tasks, matrix $\mathbf{A}$ can be replaced by an identity matrix $\mathbf{I}$, which further simplifies the computation. In this paper, the reduced-order nonlinear dynamical equation (3.25) is solved numerically with AUTO (Doedel et al., 1997), a continuation package.

4. Finite element implementation

In this section some finite element implementation considerations specifically related to the perturbation algorithm are introduced. Since the only distinction between the mechanical and the thermal loading cases is that for the former, the unit load potential $\Psi[u]$ is a quadratic implicit function of the generalized displacement field u, while for the latter, $\Psi[u]$ is linearly proportional to the unit external load pattern $\hat{p}$, i.e., $\Psi[u] = \hat{p}u$, here we will only focus on the thermoelastical model. In fact, most formulas derived for the thermal loading case also apply to the mechanical one by simply letting the thermal expansion coefficient $\alpha = 0$.

4.1. Kinematical relations

In a Cartesian coordinate system (x, y, z), consider a rectangular plate with in-plane dimensions L_a and L_b and constant thickness h in the presence of a uniformly distributed temperature field $\Delta T(x, y) = \Delta T$.

The displacement field of the mid-surface of the plate can be written in a vector form with components representing the displacements in the three coordinate directions. That is, $\mathbf{u} = \mathbf{u}(x, y) = \{u_1, u_2, u_3\}^{\mathrm{T}}$, where the components u_i designate "the functional degrees of freedom". The in-plane strains $\boldsymbol{\epsilon}(\mathbf{u}) = \{\epsilon_x, \epsilon_y, \epsilon_{xy}\}^{\mathrm{T}}$ are assumed to be governed by the von Kármán strain–displacement relations and Kirchhoff–Love's assumptions are used to determine the through-the-thickness distribution of the in-plane strain. This provides

$$\boldsymbol{\epsilon}(\mathbf{u}) = \boldsymbol{\epsilon}^{\mathrm{c}}(\mathbf{u}) + z\boldsymbol{\kappa}^{\mathrm{c}}(\mathbf{u}), \tag{4.1}$$

where $\boldsymbol{\epsilon}^{\mathrm{c}}(\mathbf{u})$ and $\boldsymbol{\kappa}^{\mathrm{c}}(\mathbf{u})$ represent the mid-surface strains and curvatures, respectively, which can be further defined as

$$\boldsymbol{\epsilon}^{\mathrm{c}}(\mathbf{u}) = \boldsymbol{\epsilon}^{\mathrm{l}}(\mathbf{u}) + \frac{1}{2}\boldsymbol{\epsilon}^{\mathrm{n}}(\mathbf{u}, \mathbf{u}), \tag{4.2}$$

$$\boldsymbol{\kappa}^{\mathrm{c}}(\mathbf{u}) = \{-u_{3,xx}, -u_{3,yy}, -2u_{3,xy}\}^{\mathrm{T}}, \tag{4.3}$$

and where subscripts denote partial differentiation with respect to the variable, for example, $(\,)_{,xy} = \partial^2(\,)/\partial x \partial y$. The linear and nonlinear parts of the in-place strain $\boldsymbol{\epsilon}^{\mathrm{c}}(\mathbf{u})$ are defined by the following expressions:

$$\boldsymbol{\epsilon}^{\mathrm{l}}(\mathbf{u}) = \{u_{1,x} + z_{\mathrm{p},x}u_{3,x}, u_{2,y} + z_{\mathrm{p},y}u_{3,y}, u_{1,y} + u_{2,x} + z_{\mathrm{p},x}u_{3,y} + z_{\mathrm{p},y}u_{3,x}\}, \tag{4.4}$$

$$\boldsymbol{\epsilon}^{\mathrm{n}}(\mathbf{u}, \mathbf{v}) = \{u_{3,x}v_{3,x}, u_{3,y}v_{3,y}, u_{3,x}v_{3,y} + u_{3,y}v_{3,x}\}^{\mathrm{T}}, \tag{4.5}$$

where z_{p} is the out-of-plane initial imperfection of the plate in the u_3 direction. It can be observed that $\boldsymbol{\epsilon}^{\mathrm{l}}(\,)$ is a linear operator while $\boldsymbol{\epsilon}^{\mathrm{n}}(\,)$ is a bi-linear operator, because

$$\boldsymbol{\epsilon}^{\mathrm{n}}(\mathbf{u}, \mathbf{v}) = \boldsymbol{\epsilon}^{\mathrm{n}}(\mathbf{v}, \mathbf{u}), \tag{4.6}$$

$$\boldsymbol{\epsilon}^{\mathrm{n}}(\mathbf{u} + \mathbf{v}, \mathbf{w}) = \boldsymbol{\epsilon}^{\mathrm{n}}(\mathbf{u}, \mathbf{w}) + \boldsymbol{\epsilon}^{\mathrm{n}}(\mathbf{v}, \mathbf{w}). \tag{4.7}$$

4.2. Potential energy and its variational expressions

The total potential energy of a thermally loaded plate is

$$\begin{aligned}\Pi[\Delta T, u] &= \Phi[u] - \Delta T \Psi[u] \\ &= \frac{1}{2}\int\int_A \left(\boldsymbol{\epsilon}^{\mathrm{l}}(\mathbf{u}) + \frac{1}{2}\boldsymbol{\epsilon}^{\mathrm{n}}(\mathbf{u}, \mathbf{u})\right)^{\mathrm{T}} \mathbf{C}\left(\boldsymbol{\epsilon}^{\mathrm{l}}(\mathbf{u}) + \frac{1}{2}\boldsymbol{\epsilon}^{\mathrm{n}}(\mathbf{u}, \mathbf{u})\right)\mathrm{d}A + \frac{1}{2}\int\int_A \boldsymbol{\kappa}^{\mathrm{c}}(\mathbf{u})^{\mathrm{T}}\mathbf{D}\boldsymbol{\kappa}^{\mathrm{c}}(\mathbf{u})\mathrm{d}A \\ &\quad - \Delta T \int\int_A \left(\boldsymbol{\epsilon}^{\mathrm{l}}(\mathbf{u}) + \frac{1}{2}\boldsymbol{\epsilon}^{\mathrm{n}}(\mathbf{u}, \mathbf{u})\right)^{\mathrm{T}} \mathbf{h}\,\mathrm{d}A,\end{aligned} \tag{4.8}$$

where material stiffness matrix $\mathbf{C}$, flexural rigidity matrix $\mathbf{D}$ and in-plane unit thermal stress vector $\mathbf{h}$ are defined by

$$\mathbf{C} = \frac{Eh}{1-\nu^2}\begin{bmatrix} 1 & \nu & 0 \\ \nu & 1 & 0 \\ 0 & 0 & \frac{1-\nu}{2} \end{bmatrix}, \quad \mathbf{D} = \frac{Eh^3}{12(1-\nu^2)}\begin{bmatrix} 1 & \nu & 0 \\ \nu & 1 & 0 \\ 0 & 0 & \frac{1-\nu}{2} \end{bmatrix}, \quad \mathbf{h} = \frac{Eh\alpha}{1-\nu}\begin{Bmatrix} 1 \\ 1 \\ 0 \end{Bmatrix}, \tag{4.9}$$

and where E represents the elastic modulus, ν represents Poison's ratio and α represents the thermal expansion coefficient.

With the strain operator defined in (4.4) and (4.5), the Frechét derivatives of $\boldsymbol{\epsilon}^{\mathrm{l}}(\mathbf{u})$, $\boldsymbol{\epsilon}^{\mathrm{n}}(\mathbf{u}, \mathbf{u})$ and $\boldsymbol{\kappa}^{\mathrm{c}}(\mathbf{u})$ can be shown to be

$$\begin{aligned}
&\boldsymbol{\epsilon}^{\mathrm{l}'}(\mathbf{u})\mathbf{q} = \boldsymbol{\epsilon}^{\mathrm{l}}(\mathbf{q}), \quad \boldsymbol{\epsilon}^{\mathrm{l}''}(\mathbf{u})\mathbf{qr} = 0,\\
&\boldsymbol{\kappa}^{\mathrm{c}'}(\mathbf{u})\mathbf{q} = \boldsymbol{\kappa}^{\mathrm{c}}(\mathbf{q}), \quad \boldsymbol{\kappa}^{\mathrm{c}''}(\mathbf{u})\mathbf{qr} = 0,\\
&\boldsymbol{\epsilon}^{\mathrm{n}'}(\mathbf{u},\mathbf{u})\mathbf{q} = 2\boldsymbol{\epsilon}^{\mathrm{n}}(\mathbf{u},\mathbf{q}), \quad \boldsymbol{\epsilon}^{\mathrm{n}''}(\mathbf{u},\mathbf{u})\mathbf{qr} = 2\boldsymbol{\epsilon}^{\mathrm{n}}(\mathbf{q},\mathbf{r}).
\end{aligned} \tag{4.10}$$

To this end, the first four Frechét derivatives of the total potential energy can be obtained as

$$\begin{aligned}
\Pi'[u]q = &\int\int_A \left(\boldsymbol{\epsilon}^{\mathrm{l}}(\mathbf{u}) + \frac{1}{2}\boldsymbol{\epsilon}^{\mathrm{n}}(\mathbf{u},\mathbf{u})\right)^{\mathrm{T}} \mathbf{C}(\boldsymbol{\epsilon}^{\mathrm{l}}(\mathbf{q}) + \boldsymbol{\epsilon}^{\mathrm{n}}(\mathbf{u},\mathbf{q}))\mathrm{d}A + \int\int_A \boldsymbol{\kappa}^{\mathrm{c}}(\mathbf{u})^{\mathrm{T}}\mathbf{D}\boldsymbol{\kappa}^{\mathrm{c}}(\mathbf{q})\mathrm{d}A - \Delta T\\
&\times \int\int_A (\boldsymbol{\epsilon}^{\mathrm{l}}(\mathbf{q}) + \boldsymbol{\epsilon}^{\mathrm{n}}(\mathbf{u},\mathbf{q}))^{\mathrm{T}}\mathbf{h}\,\mathrm{d}A,
\end{aligned} \tag{4.11}$$

$$\begin{aligned}
\Pi''[u]qr = &\int\int_A \{\boldsymbol{\epsilon}^{\mathrm{l}}(\mathbf{r})^{\mathrm{T}}\mathbf{C}\boldsymbol{\epsilon}^{\mathrm{l}}(\mathbf{q}) + \boldsymbol{\kappa}^{\mathrm{c}}(\mathbf{r})^{\mathrm{T}}\mathbf{D}\boldsymbol{\kappa}^{\mathrm{c}}(\mathbf{q})\}\mathrm{d}A + \int\int_A \{\boldsymbol{\epsilon}^{\mathrm{l}}(\mathbf{r})^{\mathrm{T}}\mathbf{C}\boldsymbol{\epsilon}^{\mathrm{n}}(\mathbf{u},\mathbf{q}) + \boldsymbol{\epsilon}^{\mathrm{n}}(\mathbf{u},\mathbf{r})^{\mathrm{T}}\mathbf{C}\boldsymbol{\epsilon}^{\mathrm{l}}(\mathbf{q})\\
&+ \boldsymbol{\epsilon}^{\mathrm{n}}(\mathbf{u},\mathbf{r})^{\mathrm{T}}\mathbf{C}\boldsymbol{\epsilon}^{\mathrm{n}}(\mathbf{u},\mathbf{q})\}\mathrm{d}A\\
&+ \int\int_A \left\{\left(\boldsymbol{\epsilon}^{\mathrm{l}}(\mathbf{u}) + \frac{1}{2}\boldsymbol{\epsilon}^{\mathrm{n}}(\mathbf{u},\mathbf{u})\right)^{\mathrm{T}}\mathbf{C}\boldsymbol{\epsilon}^{\mathrm{n}}(\mathbf{r},\mathbf{q}) - \Delta T\boldsymbol{\epsilon}^{\mathrm{n}}(\mathbf{q},\mathbf{r})^{\mathrm{T}}\mathbf{h}\right\}\mathrm{d}A,
\end{aligned} \tag{4.12}$$

$$\begin{aligned}
\Phi'''[u]qrs = &\int\int_A (\boldsymbol{\epsilon}^{\mathrm{l}}(\mathbf{s}) + \boldsymbol{\epsilon}^{\mathrm{n}}(\mathbf{u},\mathbf{s}))^{\mathrm{T}}\mathbf{C}\boldsymbol{\epsilon}^{\mathrm{n}}(\mathbf{r},\mathbf{q})\mathrm{d}A + \int\int_A (\boldsymbol{\epsilon}^{\mathrm{l}}(\mathbf{r}) + \boldsymbol{\epsilon}^{\mathrm{n}}(\mathbf{u},\mathbf{r}))^{\mathrm{T}}\mathbf{C}\boldsymbol{\epsilon}^{\mathrm{n}}(\mathbf{s},\mathbf{q})\mathrm{d}A\\
&+ \int\int_A (\boldsymbol{\epsilon}^{\mathrm{l}}(\mathbf{q}) + \boldsymbol{\epsilon}^{\mathrm{n}}(\mathbf{u},\mathbf{q}))^{\mathrm{T}}\mathbf{C}\boldsymbol{\epsilon}^{\mathrm{n}}(\mathbf{s},\mathbf{r})\mathrm{d}A,
\end{aligned} \tag{4.13}$$

$$\Phi^{(\mathrm{IV})}qrst = \int\int_A (\boldsymbol{\epsilon}^{\mathrm{n}}(\mathbf{t},\mathbf{s})^{\mathrm{T}}\mathbf{C}\boldsymbol{\epsilon}^{\mathrm{n}}(\mathbf{r},\mathbf{q}) + \boldsymbol{\epsilon}^{\mathrm{n}}(\mathbf{t},\mathbf{r})^{\mathrm{T}}\mathbf{C}\boldsymbol{\epsilon}^{\mathrm{n}}(\mathbf{s},\mathbf{q}))\mathrm{d}A + \int\int_A \boldsymbol{\epsilon}^{\mathrm{n}}(\mathbf{s},\mathbf{r})^{\mathrm{T}}\mathbf{C}\boldsymbol{\epsilon}^{\mathrm{n}}(\mathbf{t},\mathbf{q})\mathrm{d}A, \tag{4.14}$$

$$\Psi''_{\mathrm{b}}qr = \int\int_A \mathbf{h}^{\mathrm{T}}\boldsymbol{\epsilon}^{\mathrm{n}}(\mathbf{q},\mathbf{u})\mathrm{d}A. \tag{4.15}$$

4.3. Finite element discretization

The post-secondary buckling and mode-jumping analysis of plates is accomplished numerically by means of a High-Continuity (HC) finite element model, which was originally proposed in Aristodemo (1985) and Daniel (1989) and was used intensively in Casciaro et al. (1992), Lanzo et al. (1995), Salernor and Casciaro (1997) and Lanzo and Garcea (1996) to analyze the post-buckling behavior of thin-walled structures. The main features of the HC approach are: the interpolated displacement field is C^1 continuous; accurate displacement and stress can be obtained with relatively small numbers of degree of freedom; and it can avoid the 'locking phenomenon' whereby the structure tends to behave as if it is internally constrained and the accuracy of the solution is destroyed (Lanzo et al., 1995).

In the HC model (see Fig. 1), the displacement components (u_1, u_2, u_3) are interpolated from the nodal values of the nine neighboring elements based on bi-quadratic shape functions. That is

$$u_i = \sum_{j=1}^{3}\sum_{k=1}^{3} \phi_j(\xi)\phi_k(\eta)d_{ui}^{jk}, \quad \text{or} \quad u_i = \mathbf{N}\mathbf{d}_{ui}, \quad i = 1,2,3, \tag{4.16}$$

where d_{ui}^{jk}'s denote nodal values corresponding to u_i, $\mathbf{d}_{ui}^{e} = \{d_{ui}^{11}, d_{ui}^{12}, \ldots, d_{ui}^{21}, \ldots, d_{ui}^{33}\}^{\mathrm{T}}$, shape functions $\phi_i(\xi)$'s and its vector equivalent $\mathbf{N}$ are defined as

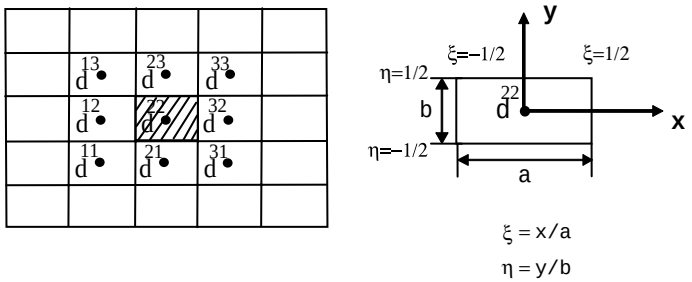

Fig. 1. High-Continuity finite element discretization.

$$\phi_1(\xi) = \frac{1}{8} - \frac{\xi}{2} + \frac{\xi^2}{2}, \quad \phi_2(\xi) = \frac{3}{4} - \xi^2, \quad \phi_3(\xi) = \frac{1}{8} + \frac{\xi}{2} + \frac{\xi^2}{2}, \tag{4.17}$$

$$\mathbf{N} = \{N_1, N_2, \ldots, N_9\}^{\mathrm{T}}, \quad N_m = \phi_j(\xi)\phi_k(\eta), \tag{4.18}$$

where $m = 3(j-1) + k$, $j, k = 1, 2, 3$.

Assuming the nodal value $\mathbf{d}_u$ in a typical element takes the form of $\mathbf{d}_u = \{\mathbf{d}_{u1}^{\mathrm{T}}, \mathbf{d}_{u2}^{\mathrm{T}}, \mathbf{d}_{u3}^{\mathrm{T}}\}^{\mathrm{T}}$, the displacement field and initial imperfection in that element can be expressed as

$$\mathbf{u} = \begin{bmatrix} \mathbf{N} & & \\ & \mathbf{N} & \\ & & \mathbf{N} \end{bmatrix} \mathbf{d}_u, \quad z_{\mathrm{p}} = \mathbf{N}\mathbf{d}_{p3}.$$

The linear and nonlinear strain operators defined in (4.3)–(4.5) thus have the following properties expressed in nodal values corresponding to the appropriate displacements:

$$\boldsymbol{\kappa}^{\mathrm{c}}(\mathbf{u}) = \mathbf{B}_{\mathrm{b}}\mathbf{d}_u, \tag{4.19}$$

$$\boldsymbol{\epsilon}^{\mathrm{l}}(\mathbf{u}) = \mathbf{B}_{\mathrm{l}}\mathbf{d}_u, \tag{4.20}$$

$$\boldsymbol{\epsilon}^{\mathrm{n}}(\mathbf{u}, \mathbf{v}) = \mathbf{B}_{\mathrm{n}}(\mathbf{u})\mathbf{d}_v = \mathbf{B}_{\mathrm{n}}(\mathbf{v})\mathbf{d}_u, \tag{4.21}$$

where

$$\mathbf{B}_{\mathrm{b}} = -\begin{bmatrix} \mathbf{0} & \mathbf{0} & \mathbf{N}_{,xx} \\ \mathbf{0} & \mathbf{0} & \mathbf{N}_{,yy} \\ \mathbf{0} & \mathbf{0} & 2\mathbf{N}_{,xy} \end{bmatrix}, \quad \mathbf{B}_{\mathrm{l}} = \begin{bmatrix} \mathbf{N}_{,x} & \mathbf{0} & z_{\mathrm{p},x}\mathbf{N}_{,x} \\ \mathbf{0} & \mathbf{N}_{,y} & z_{\mathrm{p},y}\mathbf{N}_{,y} \\ \mathbf{N}_{,y} & \mathbf{N}_{,x} & z_{\mathrm{p},x}\mathbf{N}_{,y} + z_{\mathrm{p},y}\mathbf{N}_{,x} \end{bmatrix}, \quad \mathbf{B}_{\mathrm{n}}(\mathbf{u}) = \begin{bmatrix} \mathbf{0} & \mathbf{0} & u_{3,x}\mathbf{N}_{,x} \\ \mathbf{0} & \mathbf{0} & u_{3,y}\mathbf{N}_{,y} \\ \mathbf{0} & \mathbf{0} & u_{3,x}\mathbf{N}_{,y} + u_{3,y}\mathbf{N}_{,x} \end{bmatrix}.$$

Another useful property relates to the vector product of the nonlinear operator $\boldsymbol{\epsilon}^{\mathrm{n}}(\mathbf{u}, \mathbf{v})$ with a new vector $\mathbf{w} = \{\mathbf{w}_x, \mathbf{w}_y, \mathbf{w}_{xy}\}^{\mathrm{T}}$, where $\mathbf{w}$ is assumed to be given while $\mathbf{u}$ and $\mathbf{v}$ unknown. In this situation,

$$\mathbf{w}^{\mathrm{T}}\boldsymbol{\epsilon}^{\mathrm{n}}(\mathbf{u}, \mathbf{v}) = \mathbf{d}_{u3}^{\mathrm{T}}\mathbf{G}^{\mathrm{T}}\begin{bmatrix} \mathbf{w}_x & \mathbf{w}_{xy} \\ \mathbf{w}_{xy} & \mathbf{w}_y \end{bmatrix}\mathbf{G}\mathbf{d}_{v3}, \quad \text{with } \mathbf{G} = \begin{bmatrix} \mathbf{N}_{,x} \\ \mathbf{N}_{,y} \end{bmatrix}. \tag{4.22}$$

With in-plane stresses and bending curvature obtained in (4.19)–(4.21), the scalar values of the third- and fourth-order variation terms in (4.13) and (4.14) can be calculated by summing up their contributions in each element. The element tangent stiffness matrix $\mathbf{K}_T$ is determined by the second order variational expression in (4.12):

$$\Pi''[u]\delta q\delta r = \mathbf{d}_{\delta r}^{\mathrm{T}}\mathbf{K}_T\mathbf{d}_{\delta q} = \mathbf{d}_{\delta r}^{\mathrm{T}}(\mathbf{K}_0 + \mathbf{K}_{\mathrm{L}} + \mathbf{K}_\sigma)\mathbf{d}_{\delta q}, \tag{4.23}$$

where the small displacement stiffness matrix $\mathbf{K}_0$, the large displacement stiffness matrix $\mathbf{K}_L$ and the geometric stiffness matrix $\mathbf{K}_\sigma$ are defined by the first, second and third integrals in (4.12), respectively. By applying (4.19)–(4.21), the first two stiffness matrices can be obtained directly:

$$\mathbf{K}_0 = \int\int_{A^e} (\mathbf{B}_l^{\mathrm{T}}\mathbf{C}\mathbf{B}_l + \mathbf{B}_b^{\mathrm{T}}\mathbf{D}\mathbf{B}_b)\mathrm{d}A, \tag{4.24}$$

$$\mathbf{K}_L = \int\int_{A^e} (\mathbf{B}_l^{\mathrm{T}}\mathbf{C}\mathbf{B}_n(\mathbf{u}) + \mathbf{B}_n(\mathbf{u})^{\mathrm{T}}\mathbf{C}\mathbf{B}_l + \mathbf{B}_n(\mathbf{u})^{\mathrm{T}}\mathbf{C}\mathbf{B}_n(\mathbf{u}))\mathrm{d}A. \tag{4.25}$$

Let the in-plane stress resultants be

$$\mathbf{T} = \mathbf{C}\boldsymbol{\epsilon}^{\mathrm{c}} - \Delta T\mathbf{h}, \tag{4.26}$$

with the help of (4.22), the geometric matrix may be obtained as

$$\mathbf{K}_\sigma = \begin{bmatrix} \mathbf{0} & \mathbf{0} & \mathbf{0} \\ \mathbf{0} & \mathbf{0} & \mathbf{0} \\ \mathbf{0} & \mathbf{0} & \mathbf{K}_{\sigma b} \end{bmatrix}, \quad \text{with } \mathbf{K}_{\sigma b} = \int\int_{A^e} \mathbf{G}^{\mathrm{T}} \begin{bmatrix} T_x & T_{xy} \\ T_{xy} & T_y \end{bmatrix} \mathbf{G}\,\mathrm{d}A. \tag{4.27}$$

The linearized eigenvalue problem in (3.6) can be written in its discrete form as

$$\mathbf{K}_{bT}\breve{\mathbf{v}}_{bi} = -(\lambda_{bi} - \lambda_b)\mathbf{H}_b\breve{\mathbf{v}}_{bi}, \tag{4.28}$$

with $\mathbf{H}_b$ defined by $(\Phi_b'''\hat{u}_b - \Psi_b'')\breve{v}_{bi}\delta u = \mathbf{d}_{\delta u}^{\mathrm{T}}\mathbf{H}_b\breve{\mathbf{v}}_{bi}$. Substituting this expression into (4.13), (4.15), and letting

$$\mathbf{T}^{\mathrm{ln}} = \mathbf{C}(\boldsymbol{\epsilon}^{\mathrm{l}}(\hat{\mathbf{u}}_b) + \boldsymbol{\epsilon}^{\mathrm{n}}(\mathbf{u}_b, \hat{\mathbf{u}}_b)) - \mathbf{h}, \tag{4.29}$$

we have

$$\mathbf{H}_b = \mathbf{H}_{b1} + \mathbf{H}_{b2}, \tag{4.30}$$

where

$$\mathbf{H}_{b1} = \int\int_{A^e} \left[\mathbf{B}_n(\hat{\mathbf{u}}_b)^{\mathrm{T}}\mathbf{C}(\mathbf{B}_l + \mathbf{B}_n(\mathbf{u}_b)) + (\mathbf{B}_l + \mathbf{B}_n(\mathbf{u}_b))^{\mathrm{T}}\mathbf{C}\mathbf{B}_n(\hat{\mathbf{u}}_b)\right]\mathrm{d}A, \tag{4.31}$$

$$\mathbf{H}_{b2} = \begin{bmatrix} \mathbf{0} & \mathbf{0} & \mathbf{0} \\ \mathbf{0} & \mathbf{0} & \mathbf{0} \\ \mathbf{0} & \mathbf{0} & \mathbf{H}_{bb} \end{bmatrix}, \quad \text{with } \mathbf{H}_{bb} = \int\int_{A^e} \mathbf{G}^{\mathrm{T}} \begin{bmatrix} T_x^{\mathrm{ln}} & T_{xy}^{\mathrm{ln}} \\ T_{xy}^{\mathrm{ln}} & T_y^{\mathrm{ln}} \end{bmatrix} \mathbf{G}\,\mathrm{d}A. \tag{4.32}$$

In order to get the fundamental curvature $\hat{\hat{u}}_b$ and orthogonal term $\breve{\breve{w}}_{ij}$ in Eqs. (2.10) and (3.14), one needs to solve a system of linear algebraic equations with the generalized external force related to the variational expressions $(\Phi_b'''\hat{u}_b - 2\Psi_b'')\hat{u}_b\delta u$ or $\Phi_b'''\breve{v}_{bi}\breve{v}_{bi}\delta w$. Let the generalized external force $\mathbf{f}$ take the following form:

$$\mathbf{d}_{\delta s}^{\mathrm{T}}\mathbf{f} = (\Phi_b'''q - \mathrm{const}\,\Psi_b'')r\delta s, \tag{4.33}$$

with const = 0 or 2. Substituting into (4.13) and (4.15) and using the properties of the linear and nonlinear stress operators defined in (4.19)–(4.21), one gets

$$\mathbf{f} = \mathbf{f}_\phi - \mathrm{const}\,\mathbf{f}_\psi, \tag{4.34}$$

where

$$\begin{aligned}\mathbf{f}_\phi = &\int\int_{A^e} [(\mathbf{B}_l + \mathbf{B}_n(\mathbf{u}_b))^{\mathrm{T}}\mathbf{C}\boldsymbol{\epsilon}^{\mathrm{n}}(\mathbf{r}, \mathbf{q}) + \mathbf{B}_n(\mathbf{q})^{\mathrm{T}}\mathbf{C}(\boldsymbol{\epsilon}^{\mathrm{l}}(\mathbf{r}) + \boldsymbol{\epsilon}^{\mathrm{n}}(\mathbf{u}_b, \mathbf{r}))]\mathrm{d}A \\ &+ \int\int_{A^e} [\mathbf{B}_n(\mathbf{r}_b)^{\mathrm{T}}\mathbf{C}(\boldsymbol{\epsilon}^{\mathrm{l}}(\mathbf{q}) + \boldsymbol{\epsilon}^{\mathrm{n}}(\mathbf{u}_b, \mathbf{q}))]\mathrm{d}A,\end{aligned} \tag{4.35}$$

$$\mathbf{f}_{\psi} = \int\int_{A^e} \mathbf{B}_{\mathrm{n}}(\mathbf{r})^{\mathrm{T}}\mathbf{h}\mathrm{d}A. \tag{4.36}$$

Recall from (3.14), the orthogonal terms $\breve{\breve{w}}_{ij}$ are determined by

$$\Pi''_{\mathrm{b}}\breve{\breve{w}}_{ij}\delta w + \Phi'''_{\mathrm{b}}\breve{v}_{\mathrm{b}i}\breve{v}_{\mathrm{b}j}\delta w = 0, \quad \breve{\breve{w}}_{ij} \in \mathscr{W}, \quad \forall \delta w \in \mathscr{W}.$$

By introducing M Lagrange multipliers β_k, $(k = 1, 2, \ldots, \mathrm{M})$, and considering the orthogonal condition in (3.11), the above equation defined in the orthogonal subspace $\mathscr{W}$ can be transferred to a constrained equation defined in the whole admissible subspace $\mathscr{T}$:

$$\begin{cases} \Pi''_{\mathrm{b}}\breve{\breve{w}}_{ij}\delta u + \sum_{k=1}^{M}\beta_k(\Phi'''_{\mathrm{b}}\hat{u}_{\mathrm{b}} - \Psi''_{\mathrm{b}})\breve{v}_{\mathrm{b}k}\delta u = -\Phi'''_{\mathrm{b}}\breve{v}_{\mathrm{b}i}\breve{v}_{\mathrm{b}j}\delta u, \quad \forall \delta u \in \mathscr{T}, \\ (\Phi'''_{\mathrm{b}}\hat{u}_{\mathrm{b}} - \Psi''_{\mathrm{b}})\breve{v}_{\mathrm{b}k}\breve{\breve{w}}_{ij} = 0, \quad k = 1, 2, \ldots, M. \end{cases} \tag{4.37}$$

Letting $\delta u = \breve{v}_{\mathrm{b}k}$ and noticing (3.7) and (3.23), we obtain

$$\beta_k = \begin{cases} \Phi'''_{\mathrm{b}}\breve{v}_{\mathrm{b}i}\breve{v}_{\mathrm{b}j}\breve{v}_{\mathrm{b}k} & \text{if } \lambda_{\mathrm{b}k} \geqslant \lambda_{\mathrm{b}}, \\ -\Phi'''_{\mathrm{b}}\breve{v}_{\mathrm{b}i}\breve{v}_{\mathrm{b}j}\breve{v}_{\mathrm{b}k} & \text{if } \lambda_{\mathrm{b}k} < \lambda_{\mathrm{b}}. \end{cases} \tag{4.38}$$

By using the following discretization procedure:

$$\delta\mathbf{u}^{\mathrm{T}}\mathbf{K}_{\mathrm{b}}\breve{\breve{\mathbf{w}}}_{ij} = \Pi''_{\mathrm{b}}\breve{\breve{w}}_{ij}\delta u, \quad \delta\mathbf{u}^{\mathrm{T}}\mathbf{f}_{w_{ij}} = \Phi'''_{\mathrm{b}}\breve{v}_{\mathrm{b}i}\breve{v}_{\mathrm{b}j}\delta u, \quad \delta\mathbf{u}^{\mathrm{T}}\mathbf{f}_{0k} = (\Phi'''_{\mathrm{b}}\hat{u}_{\mathrm{b}} - \Psi''_{\mathrm{b}})\breve{v}_{\mathrm{b}k}\delta u, \tag{4.39}$$

$\breve{\breve{\mathbf{w}}}_{ij}$ can be solved from

$$\mathbf{K}_{\mathrm{b}}\breve{\breve{\mathbf{w}}}_{ij} = -\mathbf{f}_{w_{ij}} - \sum_{i=1}^{M}\beta_k\mathbf{f}_{0k}. \tag{4.40}$$

5. Results and discussion

5.1. Plate models and buckling loads

The methods outlined are used to analyze the mode jumping phenomenon of isotropic aluminum rectangular plates subjected to mechanical and thermal loads. Three plate models and their corresponding boundary conditions are depicted in Fig. 2.

In case MeCS, Fig. 2(b), the plate is subjected to the uniformly distributed compressive load $\lambda\widehat{P}$ with λ the load parameter, while in cases ThermSS and ThermCC, Figs. 2(c) and (d), uniformly distributed temperature increase ΔT is applied. Geometries and material properties for these three models are listed in Table 1.

For the purpose of comparison with previous research results, different geometries and material properties are selected for the mechanical and the thermal cases. It is worth noting that only practically realistic imperfection amplitudes of the plates are adopted in Table 1 according to the experimental data. For example, the maximum out-of-plane displacement of a uniaxially compressed plate is measured as 15% of the thickness in Murphy and Virgin (1997) (in fact, initial imperfection of the MeCS plate was selected such that $\mathbf{W_0} = 0.1h(\mathbf{v}_{1\mathrm{b}} + \mathbf{v}_{2\mathrm{b}} + \mathbf{v}_{3\mathrm{b}})$ in Riks et al. (1996)), whereas the experimental measurement of the ThermSS and ThermCC plates in Table 1 shows an initial center deflection of 30% of the plate thickness (not published). To show the mode component of the geometric imperfection, the lowest two linear buckling loads ($\lambda_{1\mathrm{b}}$ and $\lambda_{2\mathrm{b}}$) and the corresponding buckling modes ($\mathbf{v}_{1\mathrm{b}}$ and $\mathbf{v}_{2\mathrm{b}}$) for each of three plate models are provided in Fig. 3.

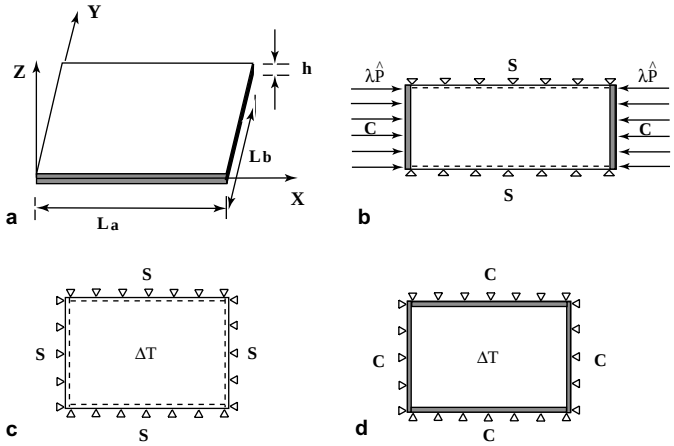

Fig. 2. Plate models and boundary conditions: (a) schematic diagram; (b) case MeCS, shorter edges clamped, longer edges simply supported and in-plane fixed; (c) case ThermSS, four edges simply supported and in-plane fixed; (d) case ThermCC, four edges clamped and in-plane fixed.

Table 1
Geometric dimensions and material properties

Parameter	Mechanical loading MeCS	Thermal loading ThermSS and ThermCC
Length L_a (mm)	644.14	762.00
Width L_b (mm)	119.63	282.22
Thickness h (mm)	1.829	1.984
Aspect ratio $r = L_a/L_b$	5.38	2.70
Young's modulus E (GPa)	70	70
Poison's ratio v	0.3	0.33
Therm-expansion coefficient α (1/°C)	23×10^{-6}	23×10^{-6}
Mass density ρ (kg/m^3)	2.790×10^3	2.714×10^3
Imperfection amplitude[a] A_0 (mm)	10%h	30%h

[a] For case MeCS, the initial imperfection has the form $\mathbf{W_0} = A_0(\mathbf{v}_{1b} + \mathbf{v}_{2b})$, while for cases ThermSS and ThermCC the form of $\mathbf{W_0} = A_0\mathbf{v}_{1b}$ is used, where $\mathbf{v}_{1b}$ and $\mathbf{v}_{2b}$ denote the first and the second linear buckling modes of the corresponding *perfect* plate, respectively. $\mathbf{v}_{1b}$ and $\mathbf{v}_{2b}$ are normalized such that $\|\mathbf{v}_{ib}\|_\infty = 1$, $i = 1,2$, where $\|\mathbf{v}_{ib}\|_\infty = \max\{\mathbf{v}_{ib} \cdot \mathbf{e}_k\}$, $k = 1,2,\ldots$

In a finite element analysis, it is desired to have convergence tests to estimate the order of mesh size necessary for the numerical solution. For this purpose, the primary and the secondary buckling load of the three plate models shown in Fig. 2 are analyzed with different mesh sizes and results are compared with other methods, see Table 2. As the convergence study shows mesh sizes 40×9 and 40×12 are sufficient for the mechanical loading and thermal loading cases, respectively, the subsequent analysis is carried out with these mesh sizes. Note that in Table 2 case MeCSfree represents the boundary conditions for Stein's experiment of a uniaxially loaded plate. Case MeCSfree, which has been studied intensively in previous publications (Audoly et al., 2002; Stoll, 1994; Riks et al., 1996; Stoll and Olson, 1997; Marcinowski, 1999), has the same geometry and material properties as those of MeCS except that the two longer edges can now move freely in the Y direction but are constrained to remain straight. From a computational point of view, multiple point constraint equations are needed to simulate the MeCSfree plate, thus more programming efforts are involved for the MeCSfree plate than those for the MeCS one. Since our aim is to

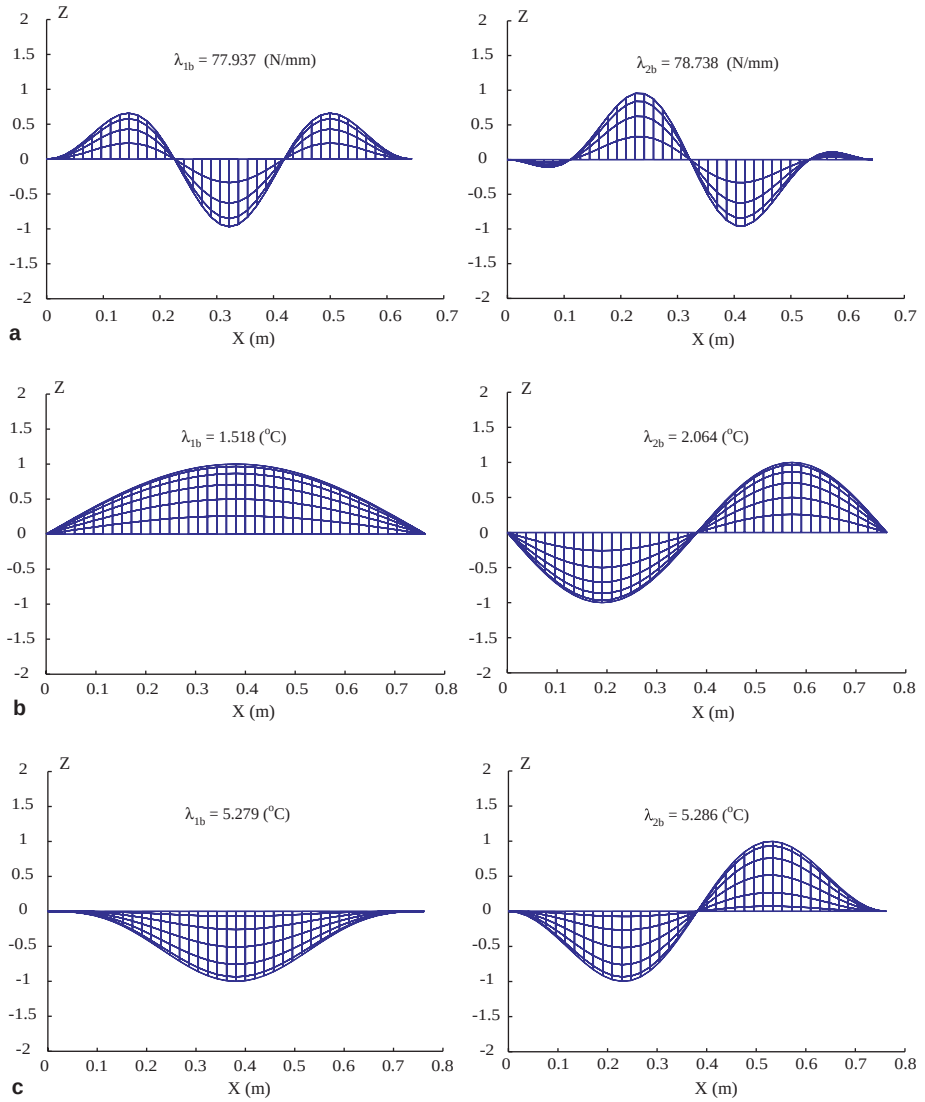

Fig. 3. The lowest two linear buckling loads and their modes of the corresponding perfect plate of the three models: (a) case MeCS, (b) case ThermSS, (c) case ThermCC.

introduce a new method to analyze the post-secondary bifurcation, for computational simplicity, the MeCS model is chosen in the present study instead of the MeCSfree one.

For a uniaxially compressed plate, the stronger the in-plane boundary constraint, the lower both the first and secondary buckling loads, with the ratio N_{b2}/N_{b1} changing slightly (from 1.84 to 1.75). N_{b1} and N_{b2} for MeCS are 25% and 29% lower than those for MeCSfree, respectively. However, for thermally loaded plates, when the out-of-plane constraint becomes stiffer, the first buckling load increases while the secondary one decreases. When compared with its mechanical counterpart, the secondary bifurcation point of the thermally loaded plate occurs much further beyond its primary buckling point, with $\Delta T_{b2}/\Delta T_{b1}$ being 9.90 in ThermCC and 44.15 in ThermSS. This may be attributed to the strong geometric effect caused by the

Table 2
Convergence test and comparison of the first and second buckling loads of three plate models

Cases	Buckling loads, 1st[a] and 2nd[b]	Present HC-element			Analytic in Chen and Virgin (2004)	ANSYS (Shell93)
		35×7	40×9	60×15		60×10
MeCS	N_{b1} (N/mm)	78.223	77.937	77.643	–	77.392
	N_{b2} (N/mm)	136.82	136.19	135.11	–	133.52
	N_{b2}/N_{b1}	1.749	1.747	1.740	–	1.725
		30×10	40×12	50×15		40×16
ThermSS	ΔT_{b1} (°C)	1.521	1.518	1.516	1.512	1.511
	ΔT_{b2} (°C)	67.44	67.04	66.73	69.31	66.36
	$\Delta T_{b2}/\Delta T_{b1}$	44.33	44.15	44.02	45.83	43.92
ThermCC	ΔT_{b1} (°C)	5.326	5.279	5.241	–	5.169
	ΔT_{b2} (°C)	51.85	52.29	51.58	–	50.55
	$\Delta T_{b2}/\Delta T_{b1}$	9.74	9.90	9.84	–	9.78

	Stein's experimental data[c]		
MeCSfree	N_{b1} (N/mm)4	N_{b2} (N/mm)	N_{b2}/N_{b1}
	103.48	191.06	1.84

[a] The first buckling load is obtained from the corresponding perfect plate.
[b] The second buckling load is the *primary* buckling load obtained in the fully geometrically nonlinear analysis of the *imperfect* plate.
[c] Converted from Stoll and Olson (1997).

boundary constraints (both in-plane and out-of-plane). Because of the intensive coupling between the external load and the displacement field, the thermally buckled plate demonstrates a stronger geometric nonlinearity than the mechanically loaded case. Therefore, the analysis of the mode jumping of the former cannot be handled easily by using the equivalent bi-axially compressed mechanical model with simple linear relations between the longitudinal and transverse edge forces.

5.2. Post-secondary bifurcation behavior

Initial post-bifurcation behavior i.e., immediately after the instability is studied by using the perturbation method. The bifurcation coefficients used for the determination of the secondary bifurcation types are obtained by using a single-mode analysis approach and results are listed in Table 3. Three typical bifurcation types—asymmetric, subcritical and supercritical, are found for plates with different combinations of load types and boundary conditions. The initial post-secondary bifurcated paths and their stability are analyzed using a multi-mode dynamic reduction method. Fig. 4 provides bifurcation diagrams for three plate models. Note that in this figure the load increment is measured from the secondary bifurcation point. It is observed from Fig. 4(a) that for the asymmetric bifurcation case, MeCS, the stable bifurcated path quickly loses its stability beyond the secondary bifurcation point, with $N_x - N_{b2} \approx 0.017.5$ (N/mm) or $\Delta N_x/N_{b1} \approx 2.45\times10^{-4}$. Therefore, strictly speaking the mode jumping occurs slightly beyond the secondary bifurcation point. It is interesting to note that for the same plate with smaller initial imperfection, say, $A_0 = 3\%h$, the bifurcation type is still asymmetric but the stable bifurcated path will never lose its stability. This means that the post-secondary bifurcation behavior of the plate is sensitive to the amplitude of the initial imperfection. This aspect will be revisited later.

Subcritical and supercritical post-secondary bifurcation behavior for thermally loaded plates are confirmed by the multi-mode reduction method, see Figs. 4(b) and (c). For case ThermSS, demonstrating sub-

Table 3
Bifurcation coefficients for three plate models

Cases	Bifurcation coefficients				Bifurcation types
	C_1	C_2	C_3	C_4	
MeCS	3.035×10^{-5}	-1	-3.2307×10^{3}	3.1342×10^{5}	Asymmetric
ThermSS	0	-1	-4.060×10^{-10}	-1.381×10^{3}	Subcritical
ThermCC	0	-1	-6.323×10^{-11}	47.552	Supercritical

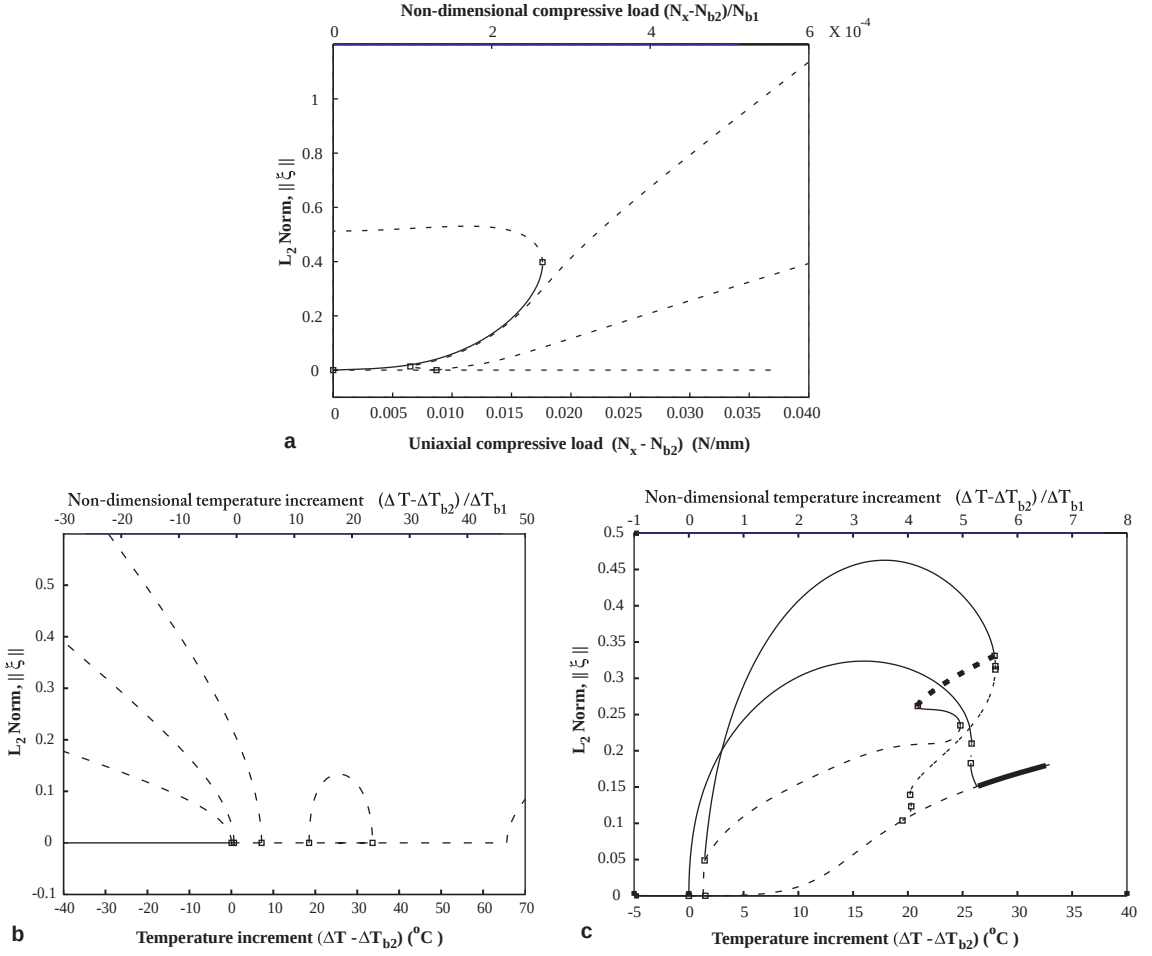

Fig. 4. Initial post-secondary bifurcation diagrams for three plate models obtained by using multi-mode dynamic reduction: (a) case MeCS, 4 modes, (b) case ThermSS, 4 modes, (c) case ThermCC, 6 modes. Stable paths are shown as solid lines and unstable paths as broken lines; $|\boldsymbol{\xi}| = \sqrt{\sum_{i=1}^{M} \xi_i^2}$.

critical bifurcation, all local post-secondary bifurcated branches are unstable. The mode jumping phenomenon is qualitatively captured for ThermCC, the supercritical one. A clearer picture of the post-secondary bifurcation and mode jumping is revealed by the load vs. displacement relations in Fig. 5. For comparison purposes, results for ThermSS are obtained by the analytic method developed in our previous paper (Chen

and Virgin, 2004) to overcome the limitations of the local perturbation approach. For the asymptotic bifurcation case, MeCS, because the stable post-secondary buckling branch loses its stability immediately after the secondary point ($\Delta N_x/N_{b1} = 2.45 \times 10^{-4}$) and the local perturbation analysis cannot capture the remote stable branch to which the plate may jump, no corresponding load vs. displacement plot is provided in Fig. 5. Fig. 5(a) exhibits a complicated post-secondary bifurcation behavior for the thermally loaded simply supported plate. Near the secondary buckling load $\Delta T_{b2} = 69.31$ °C, the bifurcation is subcritical but the unstable bifurcated paths are blocked by further bifurcation points; as a result, three unstable bifurcation paths are needed to connect the fundamental path and the remote stable target branch, demonstrating the existence of strong nonlinearity. In Fig. 5(b) the multi-mode perturbation analysis provides qualitatively the post-secondary buckling behavior of a four edges clamped plate, ThermCC. At $\Delta T_{b2} = 52.29$ °C or $\Delta T_{b2}/\Delta T_{b1} = 9.90$, two stable branches bifurcate from the secondary bifurcation point. Slightly above the bifurcated point, at $\Delta T = 53$ °C, another pair of branches emanates from the fundamental path and are initially unstable. More stable branches appear as the temperature reaches at 72 °C. Mode-jumping is observed at $\Delta T = 78$ °C, where the first pair of stable branches lose their stability and the plate will 'jump' to a remote state on one of the still stable branches. In this supercritical bifurcation case, the perturbation method can also serve as a branch-switching technique for the more accurate arc-length method—with small load increment, the displacement predicted by the former can be used as the starting point for the latter. An obvious advantage for the perturbation branch-switch is that one can control the switching procedure by selecting only stable branches. In fact, the arc-length results in Fig. 5(b) are obtained this way. When compared to arc-length, the perturbation results show good agreement up to 8 °C above the secondary bifurcation point.

Close scrutiny of Fig. 5 also reveals an interesting phenomenon: for the thermally loaded plate, after the passing of the secondary bifurcation point, stable equilibrium paths appear in pairs and each pair seems to demonstrate some kind of symmetric with respect to the fundamental path. As we will show in part II, this kind of symmetric actually reflects the fact that moving along a pair of stable paths (supercritical pair for ThermCC or the remote target one for ThermSS), the frequencies of the plate at the two corresponding points on that pair are identical.

Asymptotic analysis in this subsection shows that different combinations of boundary conditions and load types may result in different post-secondary bifurcation forms. At the secondary bifurcation point,

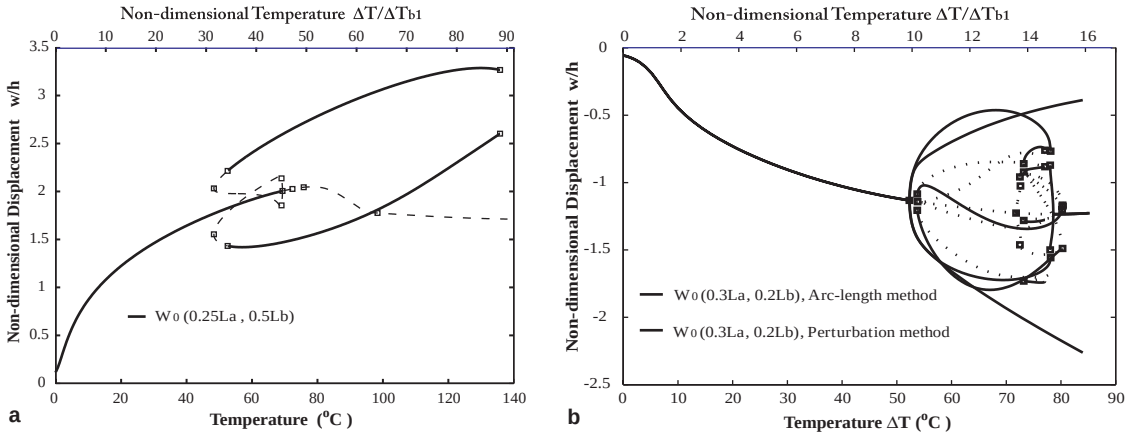

Fig. 5. Subcritical and supercritical post-secondary bifurcations for plates under thermal loading: (a) case ThermSS, analytical method using 27 global linear buckling modes (Chen and Virgin, 2004); (b) case ThermCC, perturbation method with multi-mode dynamic reduction, 6 modes. Stable paths are shown as solid lines and unstable paths as broken lines.

if the bifurcation type is determined as subcritical (meaning that all the local post-secondary paths are unstable) mode jumping happens immediately and a dramatic change of the post-buckled deformation shape can be observed. On the other hand, if an asymmetric or supercritical bifurcation type is determined, the transition of the post-buckled pattern is smooth and mode jumping may be deferred until a tertiary or higher order bifurcation points. The above results are consistent with a series of experimental observations of uniaxially compressed plates or panels. In Stein's experiment, a violent dynamic snap was observed when the configuration of an aluminum plate (with unloaded edges free to move in-plane but remaining straight) encountered a secondary instability (Stein, 1959; Stoll and Olson, 1997), while no dramatic changes of the post-buckled patterns were observed when a stiffened graphite panel (with free unloaded edges) was compressed to pass its secondary buckling load (Knight and Starnes, 1988). The final example relates to a four-edge integrated hat-stiffened composite panel under uniaxially compression. It experienced smooth propagation of post-buckled patterns until the tertiary bifurcation point was reached, where the panel exhibited a dramatic change in buckling mode shape (Falzon and Steven, 1997).

5.3. Effects of initial imperfections

Previous sections focused on the investigation of the secondary instability and mode jumping of rectangular plates under different combinations of load type and boundary conditions. The plate models are assumed to have some geometrical imperfection with reasonable imperfection amplitudes. This is a commonly used technique to study secondary instability and mode jumping phenomenon (Muheim and Johnson, 2003; Stoll, 1994; Riks et al., 1996; Stoll and Olson, 1997) and buckling in general (Murphy and Virgin, 1997). In this section, we will study the effects of the imperfection shape and the imperfection amplitude on the secondary buckling load and the initial post-secondary bifurcation behavior of the three plate models. Specifically, the initial imperfection of the plate takes one of the following two forms: $w_0 = A_0\mathbf{v}_{1b}$ and $w_0 = A_0(\mathbf{v}_{1b} + \mathbf{v}_{2b})$, where A_0 denotes the imperfection amplitude, $\mathbf{v}_{1b}$ and $\mathbf{v}_{2b}$ denote the first and the second linear buckling modes for the perfect plate. As indicated in Table 1, the maximum components of the two vectors $\mathbf{v}_{1b}$ and $\mathbf{v}_{2b}$ are normalized to be 1. For the mechanically-loaded plate, MeCS, $\mathbf{v}_{1b}$ and $\mathbf{v}_{2b}$ take the forms of the (3,1) mode and the (4,1) mode, respectively, while for the thermally-loaded ones, ThermSS and ThermCC, the (1,1) mode and the (2,1) mode are used for $\mathbf{v}_{1b}$ and $\mathbf{v}_{2b}$, respectively, see Fig. 3.

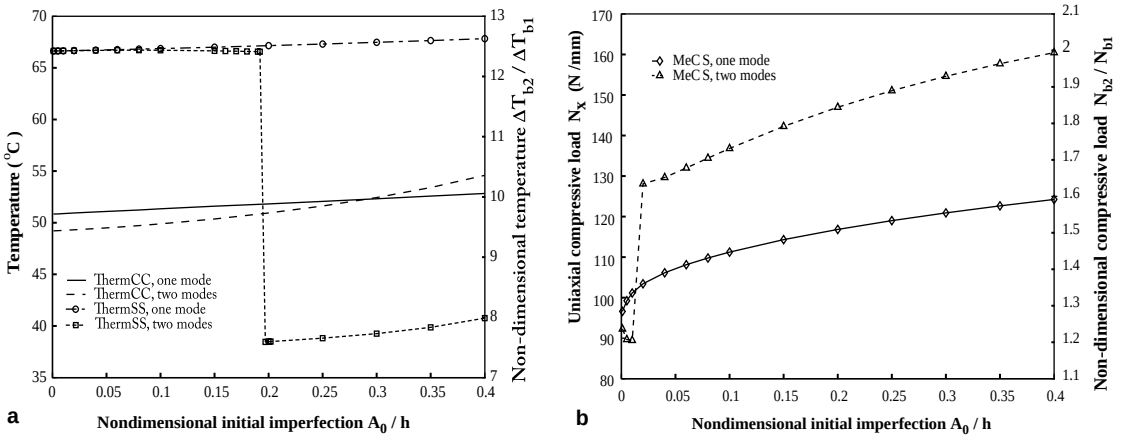

Fig. 6. The effect of initial imperfections on the secondary bifurcation loads: (a) thermal loading, cases ThermSS and ThermCC; (b) mechanical loading, case MeCS.

From Fig. 6, it can be observed that for the single-mode imperfection case the secondary bifurcation loads for three of the plate models increase monotonically with respect to the imperfection amplitude A_0, with relatively small changes of their values between $A_0/h = 0$ and $A_0/h = 0.4$. However, if the geometrical imperfection consists of two modes, the secondary bifurcation load vs. the imperfection amplitude curve may exhibit a large jump at a certain value of A_0. For MeCS, N_{b2}/N_{b1} jumps from 1.20 at $A_0 = 0.01$ to 1.64 at $A_0/h = 0.02$. Before and after this jump, N_{b2}/N_{b1} changes smoothly with respect to A_0. For ThermSS, the jump occurs around $A_0/h = 0.19$. When $A_0/h < 0.19$, the secondary buckling load T_{b2} takes the value of 67 °C and is not sensitive to the imperfection amplitude. When A_0/h is slightly larger then 0.19, T_{b2} drops dramatically to 38 °C then increases slightly and smoothly as A_0 increases. The only exception is the case ThermCC, for which T_{b2} changes slightly and smoothly as A_0/h increases from 0 to 0.4.

To this end, we will study the effect of initial imperfection on the post-secondary bifurcation behaviors of the three plate models. The post-secondary bifurcation type is determined by (2.25), using the coefficients

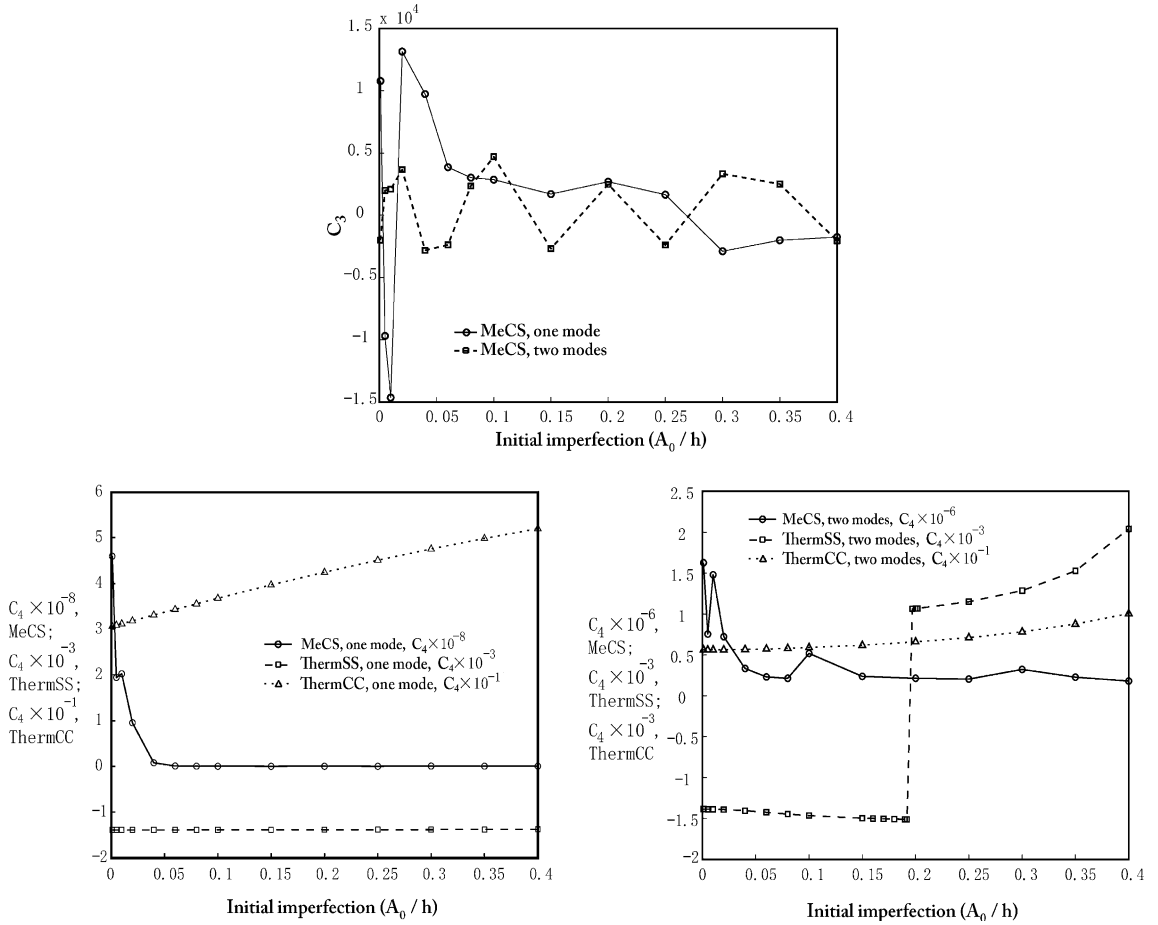

Fig. 7. The effect of initial imperfections on bifurcation coefficients: (a) coefficient C_3 for MeCS, initial imperfection consisting of one mode or two modes; (b) coefficient C_4 for three plate models, initial imperfection consisting of one mode; (c) coefficient C_4 for three plate models, initial imperfection consisting of two modes.

C_1, C_2, C_3 and C_4. Recall that in our algorithm the buckling mode is normalized to make $C_2 = -1$; C_1 is very small for MeCS and zero for ThermSS and ThermCC, as indicated in Table 3. Thus, only the coefficients C_3 and C_4 are presented in Fig. 7. In Fig. 7(a), coefficient C_3 for MeCS exhibits large values for both the single-mode and the two-mode geometrical imperfections. According to the criteria in (2.25), the post-secondary behavior for the uniaxially loaded plate is always asymmetric. Since in the range of $A_0/h = 0$–0.4 the coefficient C_3 for the thermally loaded plates (ThermSS and ThermCC) takes extremely small values (to the order of 10^{-7} and 10^{-8}, respectively), they are ignored in the determination of the bifurcation type. The thermally-loaded clamped plate, ThermCC, always exhibits the supercritical type of post-secondary bifurcation, because C_4 is always positive for both the single-mode and the two mode imperfection case. The most interesting phenomenon happens for the simply supported plate, ThermSS. Although it always demonstrates the subcritical post-secondary bifurcation if the imperfection consists of only one mode, for the two mode imperfection case the bifurcation type changes from the subcritical to supercritical as A_0/h increases above 0.19, consistent with the abrupt change of the secondary buckling load in Fig. 6(a).

The above analysis shows that both the secondary buckling load and the post-secondary bifurcation type are sensitive to initial imperfections. Thus, to improve the result for a real plate, more accurate imperfection shapes can be obtained by using a Fourier expansion of the measured surface geometries.

6. Concluding remarks

As the first stage of the systematic investigation of nonlinear post-buckling behavior (including post-buckling dynamic and mode jumping) of generalized loaded plates, an asymptotical finite element method which combines Koiter's nonlinear perturbation theory with the finite element technique is developed to study the local post-secondary bifurcation. With the utilization of a High-Continuity finite element discretization, bifurcation coefficients, which can be used to determined the post-secondary bifurcation type of the plates, are obtained by evaluating the high-order variations of the potential energy functions. A dynamical multi-mode dynamic reduction method—similar to its static single-mode counterpart: Liapunov–Schmidt reduction—is introduced. By this, the post-secondary buckling branches are obtained by solving the reduced low-dimensional parametric equations and their stability is determined directly by checking the eigenvalues of the resulting Jacobian matrix. By transferring the stability problem concerning the post-secondary bifurcated branches to that of the condensed modal parameters (ξ), this multi-mode dynamic reduction method dramatically simplifies the procedure of finding stable post-buckling paths, which is normally very complicated for many pure static approaches including the minimum potential energy method.

Different combinations of load types and boundary conditions may result in different post-secondary bifurcation form (e.g. asymmetric, supercritical and subcritical bifurcations), and consequently affect the evolution of the post-secondary buckling patterns. At the secondary bifurcation point, if the bifurcation type is determined as subcritical, mode jumping happens immediately and a dramatic change of the post-buckled deformation shape can be observed. On the other hand, if an asymmetric or supercritical bifurcation type is determined, the transition of the post-buckled pattern is smooth and mode jumping may happen later (or not at all).

Geometric imperfections are found not only to affect the secondary bifurcation load but also even to change the post-secondary bifurcation type. Because of the sensitivity of initial imperfection, it is usually preferred to perform the local post-secondary analysis before an fully dynamic investigation of the mode jumping phenomenon.

It is worth mentioning that by adopting different element types, the asymptotic finite element method developed here is applicable to analyzing more general hyperelastic problems, such as the secondary or higher order instability and mode jumping of shells. This is possible because there is no particular limitation in the development of the multi-mode dynamic reduction method.

Acknowledgement

The authors acknowledge the assistance of Professor Raffaele Casciaro of Universitá della Calabria for helpful discussions over the perturbation approach.

References

Aristodemo, M., 1985. A high-continuity finite element model for two-dimensional elastic problems. Computers and Structures 21, 987–993.

Audoly, B., 2002. Stability of straight delamination blisters. Physical Review Letters 83, 4124–4127.

Audoly, B., Roman, B., Pocheau, A., 2002. Secondary buckling patterns of a thin plate under in-plane compression. The European Physical Journal B 27, 7–10.

Budiansky, B., 1974. Theory of buckling and post-buckling behavior of elastic structures. In: Chia-Shun, Yih (Ed.), Advances in Applied Mechanicas, vol. 14. Academic Press, New York, pp. 1–65.

Casciaro, R., Lanzo, A.D., Salerno, G., 1991. Computational problems in elastic structural stability. In: Carmignani, C., Maino, G. (Eds.), Nonlinear Problems in Engineering, vol. 4. World Scientific, Singapore, pp. 66–83.

Casciaro, R., Salerno, G., Lanzo, A.D., 1992. Finite element asymptotic analysis of slender elastic structures: a simple approach. International Journal for Numerical Methods in Engineering 35, 1397–1426.

Chen, H., 2004. Nonlinear analysis of post-buckling dynamics and higher order instabilities of flexible structures. Ph.D. Dissertation, Duke University, Durham, NC, December.

Chen, H., Virgin, L.N., 2004. Dynamic analysis of modal shifting and mode jumping in thermally buckled plates. Journal of Sound and Vibration 278, 233–256.

Chen, H., Virgin, L.N., in press. Asymptotic and non-stationary finite element analysis of post-buckling dynamics in plates—Part II: Non-stationary analysis. International Journal of Solids and Structures.

Daniel, W.J.T., 1989. Performance of overlapping finite elements. Computers and Structures 31, 47–53.

Doedel, E.J., Champneys, A.R., Fairgrieve, T.F., Kuznetsov, Y.A., Sandstede, B., Wang, X.-J., 1997. AUTO97: Continuation and bifurcation software for ordinary differential equations. Technical report, Department of Computer Science, Concordia University, Montreal, Canada, 1997. Available by FTP from: <ftp.cs.concordia.ca> in directory pub/doedel/auto.

Everall, P.R., Hunt, G.W., 1999a. Arnold tongue predictions of secondary buckling in thin elastic plates. Journal of the Mechanics and Physics of Solids 47, 2187–2206.

Everall, P.R., Hunt, G.W., 1999b. Quasi-periodic buckling of an elastic structure under the influence of changing boundary conditions. Proceedings of the Royal Society of London, Series A 455, 3041–3051.

Everall, P.R., Hunt, G.W., 2000. Mode jumping in the buckling of struts and plates: a comparative study. International Journal of Non-Linear Mechanics 35, 1067–1079.

Falzon, B.G., Steven, G.P., 1997. Buckling mode transition in hat-stiffened composite panels loaded in uniaxial compression. Composite Structures 37, 253–267.

Geier, B., 2002. A method to computer Koiter's *b*-factor of anisotropic panels. International Journal of Non-Linear Mechanics 37, 699–707.

George, M., Coupeau, C., Colin, J., Cleymand, F., Grilhé, J., 2002. Delamation of metal thin films on polymer substrates: from straight-side blisters to varicose structures. Philosophical Magazine A 82, 633–641.

Hunt, G.W., Everall, P.R., 1999. Arnold tongues and mode-jumping in the supercritical post-buckling of an archetypal elastic structure. Proceedings of the Royal Society of London, Series A 455, 125–140.

Knight, N.F., Starnes Jr., J.H., 1988. Postbuckling behavior of selected curved stiffened graphite-epoxy panels loaded in axial compression. AIAA Journal 26, 344–352.

Lanzo, A.D., Garcea, G., 1996. Koiter's analysis of thin-walled structures by a finite element approach. International Journal for Numerical Methods in Engineering 39, 3007–3031.

Lanzo, A.D., Garcea, G., Casciaro, R., 1995. Asymptotic post-buckling analysis of rectangular plates by HC finite elements. International Journal for Numerical Methods in Engineering 38, 2325–2345.

Maaskant, R., Roorda, J., 1992. Mode jumping in biaxially compressed plates. International Journal of Solids and Structures 29, 1209–1219.

Marcinowski, J., 1999. Postbuckling behaviour of rectangular plates in axial compression. Archives of Civil Engineering 45, 275–288.

Muheim, D.M., Johnson, E.R., 2003. Mode jumping of an isogrid panel under quasi-static compression. In: Proceedings of the 44th AIAA/ASME/ASCE/AHS Structures, Structural Dynamics and Materials Conference, AIAA-2003-1790, Norfolk, VA, April, vol. 5, pp. 3591–3601.

Murphy, K.D., Virgin, L.N., 1997. The effect of thermal prestress on the free vibration characteristics of clamped rectangular plates: theory and experiment. Journal of Vibration and Acoustics 119, 243–249.

Nakamura, T., Uetani, K., 1979. The secondary buckling and post-buckling behaviors of rectangular plates. International Journal of Mechanical Science 21, 265–286.

Pignataro, M., Pasca, M., Franchin, P., 2000. Post-buckling analysis of corrugated panels in the presence of multiple interacting modes. Thin-Walled Structures 36 (47–66).

Riks, E., 1984. Some computational aspects of the stability analysis of nonlinear structures. Computer Methods in Applied Mechanics and Engineering 47, 219–259.

Riks, E., Rankin, C.C., Brogan, F.A., 1996. On the solution of mode jumping phenomena in thin-walled shell structures. Computer Methods in Applied Mechanics and Engineering 136, 59–92.

Salernor, G., Casciaro, R., 1997. Mode jumping and attractive paths in multimode elastic buckling. International Journal for Numerical Methods in Engineering 40, 833–861.

Schaeffer, D.G., Golubitsky, M., 1979. Boundary conditions and mode jumping in the buckling of rectangular plates. Communications in Mathematical Physics 69, 209–236.

Sridhar, N., Srolovitz, D.J., Suo, Z., 2001. Kinetics of buckling of compressed film on a viscous substrate. Applied Physics letters 78, 2482, 2484.

Sridhar, N., Srolovitz, D.J., Cox, B.N., 2002. Buckling and post-buckling kinetics of compressed thin films on viscous substrates. Acta Materialia 50, 2547–2557.

Stein, M., 1959. Loads and deformation of buckled rectangular plates. NASA Technical Report R–40, National Aeronautics and Space Administration, 1959.

Stoll, F., 1994. Analysis of the snap phenomenon in buckled plates. International Journal of Non-Linear Mechanics 29, 123–138.

Stoll, F., Olson, S.E., 1997. Finite element investigation of the snap phenomenon in buckled plates. In: Proceedings of the 1997 38th AIAA/ASME/ASCE/AHS/ASC Structures, Structural Dynamics, and Materials Conference, vol. 4, pp. 2703–2712.

Supple, W.J., 1968. On the change in buckle pattern in elastic structures. International Journal of Mechanical Sciences 10, 737–745.

Uemura, M., Byon, O., 1977. Secondary buckling of a flat plate under uniaxial compression—Part 1: Theoretical analysis of simply supported flat plate. International Journal of Non-Linear Mechanics 12, 355–370.

Virgin, L.N., Chen, H., 2003. The dynamics of mode jumping in thermally buckled plates. In: The 8th International Conference on Recent Advances in Structural Dynamics, Southampton, UK, July 2003.